Journal of Computational Physics 326 (2016) 893–912

Contents lists available at ScienceDirect

Journal of Computational Physics

www.elsevier.com/locate/jcp

A hydrodynamically-consistent MRT lattice Boltzmann model on a 2D rectangular grid

Cheng Peng [a], Haoda Min [a], Zhaoli Guo [b], Lian-Ping Wang [a,b,*]

[a] Department of Mechanical Engineering, University of Delaware, Newark, DE 19716-3140, USA
[b] State Key Laboratory of Coal Combustion, Huazhong University of Science and Technology, Wuhan, PR China

ARTICLE INFO

Article history:
Received 13 January 2016
Accepted 12 September 2016
Available online 17 September 2016

Keywords:
Lattice Boltzmann method
MRT collision operator
Rectangular grid
Navier–Stokes equations

ABSTRACT

A multiple-relaxation time (MRT) lattice Boltzmann (LB) model on a D2Q9 rectangular grid is designed theoretically and validated numerically in the present work. By introducing stress components into the equilibrium moments, this MRT-LB model restores the isotropy of diffusive momentum transport at the macroscopic level (or in the continuum limit), leading to moment equations that are fully consistent with the Navier–Stokes equations. The model is derived by an inverse design process which is described in detail. Except one moment associated with the energy square, all other eight equilibrium moments can be theoretically and uniquely determined. The model is then carefully validated using both the two-dimensional decaying Taylor–Green vortex flow and lid-driven cavity flow, with different grid aspect ratios. The corresponding results from an earlier model (Bouzidi et al. (2001) [28]) are also presented for comparison. The results of Bouzidi et al.'s model show problems associated with anisotropy of viscosity coefficients, while the present model exhibits full isotropy and is accurate and stable.

1. Introduction

Direct numerical simulations (DNS) are routinely used to study turbulent flows. In many engineering applications, turbulent flows are usually anisotropic and inhomogeneous due to, for example, solid boundary confinements. Consider DNS of a turbulent channel flow: the velocity gradients in the wall normal direction are much larger than that in the streamwise and spanwise directions. Therefore, to resolve all the details in the flow, a finer grid resolution is needed in the wall normal direction, especially in the near-wall region where the largest velocity gradients are present [1]. On the other hand, a sufficient domain length in the streamwise direction is required to realistically simulate flow statistics, especially higher-order statistics [2–5]. These two considerations call for different grid resolutions in different spatial directions, as often configured in conventional or macroscopic computational fluid dynamics (CFD) methods based on directly solving the Navier–Stokes (N–S) equations [2,6].

In the last three decades, the lattice Boltzmann method (LBM) has been rapidly developed as a mesoscopic approach to solve fluid flows in the continuum limit. With its simplicity of implementation, flexibility of boundary treatments, as well as excellent parallel-computing capability, LBM has been proven to be an efficient tool for large-scale flow simula-

* Corresponding author at: Department of Mechanical Engineering, University of Delaware, Newark, DE 19716-3140, USA.
E-mail addresses: cpengxpp@udel.edu (C. Peng), min@udel.edu (H. Min), zlguo@hust.edu.cn (Z. Guo), lwang@udel.edu (L.-P. Wang).

http://dx.doi.org/10.1016/j.jcp.2016.09.031
0021-9991/

tions, especially for those with multiple flow scales and complex geometries, such as turbulent flows laden with finite-size particles [7–11].

Indeed, LBM models incorporating non-uniform or irregular meshes have been considered to improve the competitiveness of this mesoscopic approach, when compared to the conventional CFD methods. Local grid-refinement techniques, for example, have been developed for LBM [12–17], where a dense grid is embedded for certain portions of the computational domain. Relationships between the distribution functions at two different mesh resolutions have been developed to exchange information at the coarse-fine grid interfaces, in a manner that maintains the continuity of hydrodynamic variables (*e.g.*, velocity, pressure, viscosity, stress). This approach has been widely used in LBM applications involving, for example, moving fluid–solid interfaces [9,18–21].

Alternatively, the streaming step in LBM can be decoupled from the lattice grid, by either using interpolation [22–24] or introducing finite difference/finite volume schemes [25,26]. When the interpolation is used to map off-grid distributions to the on-grid distributions, the accuracy of the simulation is still constrained by the resolution of the inherent lattice grid, and additional errors and numerical dissipation are introduced by the interpolation. Incorporating finite difference/finite volume schemes into LBM also introduces additional numerical diffusion and dispersion to the flow. Usually, those schemes are also more complicated than the regular LBM, making the implementation more difficult.

The direct extension of LBM to an anisotropic mesh is therefore preferred, but requires a re-design of the collision operation. The very first effort in this direction was the work of Koelman [27], who proposed a lattice Bhatnagar–Gross–Krook (BGK) model on a rectangular grid, by employing a low Mach-number expansion of the Maxwell–Boltzmann equilibrium distribution to obtain the equilibrium distribution on rectangular lattices. Although his model can calculate hydrodynamic variables correctly, it fails to recover the N–S equations with isotropic transport coefficients when the grid aspect ratio a is different from one [28]. Inspired by the work of Koelman, Bouzidi et al. [28] proposed a multiple-relaxation time (MRT) LB model on a D2Q9 (two-dimension nine-velocity) rectangular grid. Utilizing the greater flexibility in MRT LBM, this model partly eliminates the previous anisotropy problem by coupling properly the relaxation parameters of the energy and normal stress moments to that of shear stress moment. Although this model yielded correct results in several test cases, it was later shown to be not fully isotropic [29]. Two other attempts were made by Zhou [30,31], who considered both lattice BGK and MRT models on a D2Q9 rectangular grid [30,31]. Like Bouzidi et al.'s model, Zhou's models do not recover the correct hydrodynamics, as shown in [29,32]. Hegele et al. [33] concluded that, for the popular D2Q9 lattice and D3Q19 (three-dimension nineteen-velocity) lattice, the degrees of freedom are not enough to cancel out the anisotropy resulting from the use of anisotropic lattice, when the BGK collision operator is used. Thus they suggested that lattice BGK models on D2Q11 and D3Q23 lattice grids can successfully recover the isotropic stress tensor, although the detailed Chapman–Enskog analysis was not presented. Their D2Q11 model was validated using the 2D Taylor–Green vortex flow, but no numerical validation was shown for the D3Q23 model. Hegele et al. [33] incorrectly stated that Bouzidi's model could reproduce the N–S equations.

Recently, Zong et al. [29] (thereafter the θ model) proposed another MRT LBM on a D2Q9 rectangular grid, in which the energy and normal stress moments in Bouzidi et al.'s model were coupled through an additional parameter θ which is related to the rotation angle of the corresponding two-dimensional moment sub-space. Using this additional degree of freedom, Zong et al. were able to fully restore the isotropy and reproduced the exact N–S equations. The model was validated using both the lid-driven cavity flow and the Taylor–Green vortex flow.

In this work, an alternative and more general approach is explored to design a MRT LB model on a D2Q9 rectangular grid. The basic idea is to introduce stress components into the equilibrium moments to offset the anisotropy in the stress tensor resulting from the use of a rectangular lattice. This approach was previously used by Inamuro [34] to improve the stability of lattice BGK model, which allowed the relaxation time to be tuned independent of the viscosity. In this manner, flows at higher Reynolds numbers (Re) can be simulated. Later, Yoshino et al. [35] applied the same idea to simulate non-Newtonian fluid flows, where the local viscosity depends on the local flow strain rate. Wang et al. [36] further improved Yoshino et al.'s work by ensuring the local mass-conservation in the approach. Recently, Meng and Guo developed a MRT model for miscible flows with large viscosity ratios and Peclet numbers, in which the stress is incorporated in the equilibrium moments [37].

Compared with the θ model, the present model has several preferable features. First, all leading-order equilibrium moments are unchanged, so the model is simpler and more concise, making it easier to be extended to other lattice types, *e.g.*, 3D lattice grids. Second, the present model inherits the feature in [34–36] that the relaxation time can be adjusted, independent of the flow viscosities. Therefore, it has more flexibility than the θ model in terms of the numerical stability and the range of flow Reynolds numbers that can be simulated.

The remainder of the paper is arranged as follows. In Sec. 2, a detailed inverse design analysis of a new MRT LB model is presented. General guidelines for setting adjustable parameters in the proposed model are provided in Sec. 3. In Sec. 4, the present model will be validated using a steady 2D lid-driven cavity flow and an unsteady decaying Taylor–Green vortex flow. Section 5 contains a summary of main conclusions and an outlook.

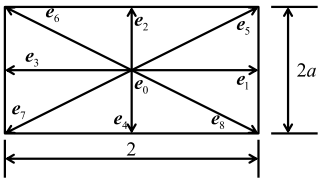

Fig. 1. Discrete velocities of the D2Q9 rectangular lattice grid.

2. Derivation of an MRT LB model on a rectangular grid

2.1. The basic model setup

We first describe the basic model setup, which are similar to those discussed in [28,29]. The nine discrete velocities $\mathbf{e}_i$ for a rectangular D2Q9 lattice grid are shown in Fig. 1, which are

$$\mathbf{e}_i = \begin{cases} (0,0)c, & i=0, \\ (\pm 1,0)c, & i=1,3, \\ (0,\pm a)c, & i=2,4, \\ (\pm 1,\pm a)c, & i=5\text{–}8, \end{cases} \tag{1}$$

where $a=\delta_y/\delta_x$ is the grid aspect ratio for the rectangular lattice, $c=\delta_x/\delta_t$ is the lattice velocity [$\mathrm{m}\cdot\mathrm{s}^{-1}$] in the x direction, δ_x [m] and δ_y [m] are lattice spacings in the x and y directions, respectively, and δ_t [s] is the time step size. Physical units are explicitly stated here to help check the consistency of our derivations.

In the MRT models, the collision relaxation is applied to moments, and the lattice Boltzmann equation is written as [38,39]

$$\mathbf{f}(\mathbf{x}+\mathbf{e}_i\delta_t, t+\delta_t) - \mathbf{f}(\mathbf{x},t) = -\mathbf{M}^{-1}\mathbf{S}\left[\mathbf{m}(\mathbf{x},t) - \mathbf{m}^{(eq)}(\mathbf{x},t)\right], \tag{2}$$

where $\mathbf{x}$ and t are the spatial and time coordinate, respectively. $\mathbf{f}$ [$\mathrm{kg}\cdot\mathrm{m}^{-3}$] denotes the distribution function vector associated with the discrete velocities $\mathbf{e}_i$. The matrix $\mathbf{M}$ (and its inverse $\mathbf{M}^{-1}$) transforms the distribution functions to moments as

$$\mathbf{m}=\mathbf{M}\mathbf{f}, \quad \mathbf{f}=\mathbf{M}^{-1}\mathbf{m}. \tag{3}$$

The vector $\mathbf{m}$ contains 9 components, namely,

$$\mathbf{m} = \left|\rho, e, \varepsilon, j_x, q_x, j_y, q_y, p_{xx}, p_{xy}\right\rangle, \tag{4}$$

where the ρ is the density, e is related to the kinetic energy, ε is related to energy square; j_x and j_y are the momentum in x and y directions, respectively; q_x and q_y are associated with the x and y components of energy flux, respectively; p_{xx} and p_{xy} are the moments related to the normal and shear stress, respectively. The equilibrium moments $\mathbf{m}^{(eq)}$ are functions of the conserved moments *i.e.*, ρ, j_x, and j_y, whose exact forms will be determined by an inverse design analysis. $\mathbf{S}$ is the diagonal relaxation matrix $\mathbf{S}=diag\left(s_\rho, s_e, s_\varepsilon, s_j, s_q, s_j, s_q, s_n, s_c\right)$, where each element controls the relaxation rate of a given moment and has been normalized by the time step size.

Similar to the previous studies [28,29], the transform matrix $\mathbf{M}$ in the present model is defined as

$$\mathbf{M} = \begin{bmatrix} 1 & 1 & 1 & 1 & 1 & 1 & 1 & 1 & 1 \\ -2r_1 & r_2 & r_3 & r_2 & r_3 & r_1 & r_1 & r_1 & r_1 \\ 4 & -2 & -2 & -2 & -2 & 1 & 1 & 1 & 1 \\ 0 & 1 & 0 & -1 & 0 & 1 & -1 & -1 & 1 \\ 0 & -2 & 0 & 2 & 0 & 1 & -1 & -1 & 1 \\ 0 & 0 & a & 0 & -a & a & a & -a & -a \\ 0 & 0 & -2a & 0 & 2a & a & a & -a & -a \\ -2r_4 & r_5 & r_6 & r_5 & r_6 & r_4 & r_4 & r_4 & r_4 \\ 0 & 0 & 0 & 0 & 0 & 1 & -1 & 1 & -1 \end{bmatrix}, \tag{5}$$

where $r_1=a^2+1$, $r_2=1-2a^2$, $r_3=a^2-2$, $r_4=a^2-1$, $r_5=a^2+2$, $r_6=-1-2a^2$. The rows of the $\mathbf{M}$ matrix are orthogonal to one another.

Accordingly, the inverse matrix $\mathbf{M}^{-1}$ is simply the transpose of $\mathbf{M}$, with a proper normalization for each column of $\mathbf{M}^{-1}$. It is given as

$$\mathbf{M}^{-1}=\begin{bmatrix}
\frac{1}{9} & -\frac{r_1}{9r_7} & \frac{1}{9} & 0 & 0 & 0 & 0 & -\frac{r_4}{9r_7} & 0\\
\frac{1}{9} & \frac{r_2}{18r_7} & -\frac{1}{18} & \frac{1}{6} & -\frac{1}{6} & 0 & 0 & \frac{r_5}{18r_7} & 0\\
\frac{1}{9} & \frac{r_3}{18r_7} & -\frac{1}{18} & 0 & 0 & \frac{1}{6a} & -\frac{1}{6a} & \frac{r_6}{18r_7} & 0\\
\frac{1}{9} & \frac{r_2}{18r_7} & -\frac{1}{18} & -\frac{1}{6} & \frac{1}{6} & 0 & 0 & \frac{r_5}{18r_7} & 0\\
\frac{1}{9} & \frac{r_3}{18r_7} & -\frac{1}{18} & 0 & 0 & -\frac{1}{6a} & \frac{1}{6a} & \frac{r_6}{18r_7} & 0\\
\frac{1}{9} & \frac{r_1}{18r_7} & \frac{1}{36} & \frac{1}{6} & \frac{1}{12} & \frac{1}{6a} & \frac{1}{12a} & \frac{r_4}{18r_7} & \frac{1}{4}\\
\frac{1}{9} & \frac{r_1}{18r_7} & \frac{1}{36} & -\frac{1}{6} & -\frac{1}{12} & \frac{1}{6a} & \frac{1}{12a} & \frac{r_4}{18r_7} & -\frac{1}{4}\\
\frac{1}{9} & \frac{r_1}{18r_7} & \frac{1}{36} & -\frac{1}{6} & -\frac{1}{12} & -\frac{1}{6a} & -\frac{1}{12a} & \frac{r_4}{18r_7} & \frac{1}{4}\\
\frac{1}{9} & \frac{r_1}{18r_7} & \frac{1}{36} & \frac{1}{6} & \frac{1}{12} & -\frac{1}{6a} & -\frac{1}{12a} & \frac{r_4}{18r_7} & -\frac{1}{4}
\end{bmatrix}, \tag{6}$$

where $r_7=a^4+1$. Note that the row vectors of $\mathbf{M}$ are orthogonal, and the column vectors of $\mathbf{M}^{-1}$ are orthogonal.

2.2. The inverse design analysis

In this subsection, we shall build a new MRT-LB model by following the same inverse design procedure as described in [29]. Multiplying Eq. (2) by the transform matrix $\mathbf{M}$, and applying Taylor expansion to the left-hand side (LHS) of the equation, we can write the evolution function in terms of moments as

$$\hat{\mathbf{D}}\mathbf{m}+\frac{\delta_t}{2}\hat{\mathbf{D}}^2\mathbf{m}=-\frac{\mathbf{S}}{\delta_t}\left[\mathbf{m}-\mathbf{m}^{(eq)}\right], \tag{7}$$

where $\hat{\mathbf{D}}=\mathbf{I}\partial_t+\hat{\mathbf{C}}_\alpha\nabla_\alpha=\mathbf{I}\partial_t+\mathbf{M}\mathbf{C}_\alpha\mathbf{M}^{-1}\nabla_\alpha$, $\mathbf{I}$ is an identity matrix and $\mathbf{C}_\alpha$ is the diagonal matrix containing $e_{i\alpha}$. The index α denotes the spatial directions.

We now perform a Chapman–Enskog multiscaling analysis to derive the moment equations. The moments $\mathbf{m}$, the time and spatial derivatives in Eq. (7) are expanded as

$$\mathbf{m}=\mathbf{m}^{(0)}+\epsilon\mathbf{m}^{(1)}+\epsilon^2\mathbf{m}^{(2)}+\cdots, \tag{8a}$$

$$\frac{\partial}{\partial t}=\epsilon\partial_{t1}+\epsilon^2\partial_{t2}+\cdots, \tag{8b}$$

$$\nabla_\alpha\equiv\partial_\alpha=\epsilon\partial_{1\alpha}+\cdots, \tag{8c}$$

where ϵ is a small parameter proportional to the Knudsen number (*i.e.*, the ratio between molecular mean free path to the macroscopic length).

Different from the previous MRT-LB models, the equilibrium moments $\mathbf{m}^{(eq)}$ in the present model are also expanded as

$$\mathbf{m}^{(eq)}=\mathbf{m}^{(0,eq)}+\epsilon\mathbf{m}^{(1,eq)}+\cdots. \tag{9}$$

Substituting Eq. (8) and Eq. (9) into Eq. (7), and grouping the terms according to the order of ϵ, we obtain

$$\mathcal{O}(1):\quad \mathbf{m}^{(0)}=\mathbf{m}^{(0,eq)}, \tag{10a}$$

$$\mathcal{O}(\epsilon):\quad \left(\mathbf{I}\partial_{t1}+\hat{\mathbf{C}}_\alpha\partial_{1\alpha}\right)\mathbf{m}^{(0)}=-\frac{\mathbf{S}}{\delta_t}\left(\mathbf{m}^{(1)}-\mathbf{m}^{(1,eq)}\right), \tag{10b}$$

$$\mathcal{O}\left(\epsilon^2\right):\quad \mathbf{I}\partial_{t2}\mathbf{m}^{(0)}+\left(\mathbf{I}\partial_{t1}+\hat{\mathbf{C}}_\alpha\partial_{1\alpha}\right)\left(\mathbf{I}-\frac{\mathbf{S}}{2}\right)\mathbf{m}^{(1)}+\left(\mathbf{I}\partial_{t1}+\hat{\mathbf{C}}_\alpha\partial_{1\alpha}\right)\frac{\mathbf{S}}{2}\mathbf{m}^{(1,eq)}=-\frac{\mathbf{S}}{\delta_t}\mathbf{m}^{(2)}. \tag{10c}$$

For the three conservative moments, as in the standard MRT LBM, we set $m_1^{(0)}=\delta\rho$ [kg·m^{-3}], $m_4^{(0)}=\rho_0 u$ [kg·m^{-2}·s^{-1}], $m_6^{(0)}=\rho_0 v$ [kg·m^{-2}·s^{-1}], where $\delta\rho$ and ρ_0 are the local density fluctuation and the constant background density per the

incompressible formulation in He and Luo [40], respectively. Without external forcing, it follows that $m_{1,4,6}^{(k)} = 0$ for $k \geq 1$. Consequently, the first, fourth and sixth rows of Eq. (10b) yield

$$\partial_{t1}\delta\rho + \partial_{1x}(\rho_0 u) + \partial_{1y}(\rho_0 v) = -\frac{s_\rho}{\delta_t}\left[-m_1^{(1,eq)}\right], \tag{11a}$$

$$\partial_{t1}(\rho_0 u) + \partial_{1x}\left[\frac{2}{3}c^2\delta\rho + \frac{1}{3r_7}m_2^{(0,eq)} + \frac{a^2}{3r_7}m_8^{(0,eq)}\right] + \partial_{1y}\left[am_9^{(0,eq)}\right] = -\frac{s_j}{\delta_t}\left[-m_4^{(1,eq)}\right], \tag{11b}$$

$$\partial_{t1}(\rho_0 v) + \partial_{1x}\left[am_9^{(0,eq)}\right] + \partial_{1y}\left[\frac{2a^2}{3}c^2\delta\rho + \frac{a^4}{3r_7}m_2^{(0,eq)} - \frac{a^2}{3r_7}m_8^{(0,eq)}\right] = -\frac{s_j}{\delta_t}\left[-m_6^{(1,eq)}\right]. \tag{11c}$$

The above equations should be designed to match the Euler equations, namely,

$$\partial_t\delta\rho + \partial_x(\rho_0 u) + \partial_y(\rho_0 v) = 0, \tag{12a}$$

$$\partial_t(\rho_0 u) + \partial_x\left(p + \rho_0 u^2\right) + \partial_y(\rho_0 uv) = 0, \tag{12b}$$

$$\partial_t(\rho_0 v) + \partial_x(\rho_0 uv) + \partial_y\left(p + \rho_0 v^2\right) = 0, \tag{12c}$$

where p $[\mathrm{kg}\cdot\mathrm{m}^{-1}\cdot\mathrm{s}^{-2}] = \delta\rho c_s^2$, c_s is the speed of sound $[\mathrm{m}\cdot\mathrm{s}^{-1}]$. It follows that all the equilibrium moments appearing in Eq. (11) can be determined and they are: $\epsilon m_1^{(1,eq)} = \epsilon m_4^{(1,eq)} = \epsilon m_6^{(1,eq)} = 0$, $m_9^{(0,eq)}$ $[\mathrm{kg}\cdot\mathrm{m}^{-1}\cdot\mathrm{s}^{-2}] = \rho_0 uv/a$, $m_2^{(0,eq)}$ $[\mathrm{kg}\cdot\mathrm{m}^{-1}\cdot\mathrm{s}^{-2}] = 2\delta\rho\left(3c_s^2 - c^2 r_1\right) + 3\rho_0\left(u^2+v^2\right)$ and $m_8^{(0,eq)}$ $[\mathrm{kg}\cdot\mathrm{m}^{-1}\cdot\mathrm{s}^{-2}] = \left(r_4/a^2\right)\left(3r_1c_s^2 - 2c^2a^2\right)\delta\rho + 3\rho_0\left(a^2u^2 - v^2/a^2\right)$.

Next, we proceed to the $\mathcal{O}(\epsilon^2)$ equations. To simplify the expressions, we set $\mathbf{A} = \left(\mathbf{I} - \frac{\mathbf{S}}{2}\right)\mathbf{m}^{(1)}$ and $\mathbf{B} = \frac{\mathbf{S}}{2}\mathbf{m}^{(1,eq)}$, where A_i and B_i have the same physical unit as m_i, in particular, A_2, B_2, A_8, B_8, A_9, B_9 all have the unit of $[\mathrm{kg}\cdot\mathrm{m}^{-1}\cdot\mathrm{s}^{-2}]$. Then Eq. (10c) becomes

$$\partial_{t2}\mathbf{m}^{(0)} + \left(\mathbf{I}\partial_{t1} + \hat{\mathbf{C}}_\alpha\partial_{1\alpha}\right)(\mathbf{A}+\mathbf{B}) = -\frac{\mathbf{S}}{\delta_t}\mathbf{m}^{(2)}. \tag{13}$$

The first, fourth and sixth rows of Eq. (13) are

$$\partial_{t2}\delta\rho = 0, \tag{14a}$$

$$\partial_{t2}(\rho_0 u) + \partial_{1x}\left[\frac{(A_2+B_2)}{3r_7} + \frac{a^2(A_8+B_8)}{3r_7}\right] + \partial_{1y}\left[a(A_9+B_9)\right] = 0, \tag{14b}$$

$$\partial_{t2}(\rho_0 v) + \partial_{1x}\left[a(A_9+B_9)\right] + \partial_{1y}\left[\frac{a^4(A_2+B_2)}{3r_7} - \frac{a^2(A_8+B_8)}{3r_7}\right] = 0. \tag{14c}$$

Eq. (14a) is consistent with the continuity equation at the higher order. Eqs. (14b) and (14c) are required to recover the viscous terms in the N–S equations, namely,

$$\begin{aligned}&\partial_{t2}(\rho_0 u) - \partial_x\left\{\nu^V\left[\partial_x(\rho_0 u) + \partial_y(\rho_0 v)\right] + \nu\left[\partial_x(\rho_0 u) - \partial_y(\rho_0 v)\right]\right\}\\ &- \partial_y\left\{\nu\left[\partial_y(\rho_0 u) + \partial_x(\rho_0 v)\right]\right\} = 0,\end{aligned} \tag{15a}$$

$$\begin{aligned}&\partial_{t2}(\rho_0 v) - \partial_y\left\{\nu^V\left[\partial_x(\rho_0 u) + \partial_y(\rho_0 v)\right] - \nu\left[\partial_x(\rho_0 u) - \partial_y(\rho_0 v)\right]\right\}\\ &- \partial_x\left\{\nu\left[\partial_y(\rho_0 u) + \partial_x(\rho_0 v)\right]\right\} = 0,\end{aligned} \tag{15b}$$

where ν $[\mathrm{m}^2\cdot\mathrm{s}^{-1}]$ is the shear viscosity and ν^V $[\mathrm{m}^2\cdot\mathrm{s}^{-1}]$ is the bulk viscosity. Therefore, matching Eq. (14) with Eq. (15), we have

$$-\nu^V\left[\partial_x(\rho_0 u) + \partial_y(\rho_0 v)\right] - \nu\left[\partial_x(\rho_0 u) - \partial_y(\rho_0 v)\right] = \frac{\epsilon(A_2+B_2)}{3r_7} + \frac{\epsilon a^2(A_8+B_8)}{3r_7}, \tag{16a}$$

$$-\nu^V\left[\partial_x(\rho_0 u) + \partial_y(\rho_0 v)\right] + \nu\left[\partial_x(\rho_0 u) - \partial_y(\rho_0 v)\right] = \frac{\epsilon a^4(A_2+B_2)}{3r_7} - \frac{\epsilon a^2(A_8+B_8)}{3r_7}, \tag{16b}$$

$$-\nu\left[\partial_y(\rho_0 u) + \partial_x(\rho_0 v)\right] = a\epsilon(A_9+B_9). \tag{16c}$$

The above equations represent our design constraints. Once all are fulfilled, the MRT-LB model shall reproduce the N–S equations exactly.

In order to impose these constraints on the equilibrium moments, we need to first determine (A_2+B_2), (A_8+B_8) and (A_9+B_9). Taking the second, eighth and ninth rows of the moment equation on the order of $\mathcal{O}(\epsilon)$, *i.e.*, Eq. (10b), we obtain that

$$\begin{aligned} A_2+B_2 &= m_2^{(1,eq)} - \left(\frac{2-s_e}{2s_e}\right)\delta_t\left\{\partial_{1x}\left[a^2 m_5^{(0,eq)}\right] + \partial_{1y} m_7^{(0,eq)}\right\} \\ &- \left(\frac{2-s_e}{2s_e}\right)\delta_t\left[\left(3c^2+2c^2a^2-6c_s^2\right)\partial_{1x}(\rho_0 u) + \left(3c^2a^2+2c^2-6c_s^2\right)\partial_{1y}(\rho_0 v)\right], \end{aligned} \tag{17a}$$

$$\begin{aligned} A_8+B_8 &= m_8^{(1,eq)} + \left(\frac{2-s_n}{2s_n}\right)\delta_t\left\{\partial_{1x} m_5^{(0,eq)} - \partial_{1y}\left[a^2 m_7^{(0,eq)}\right]\right\} \\ &- \left(\frac{2-s_n}{2s_n}\right)\delta_t\left[\left(3c^2a^2 - \frac{3r_1r_4c_s^2}{a^2} - 2c^2\right)\partial_{1x}(\rho_0 u) + \left(2c^2a^2 - 3c^2 - \frac{3r_1r_4c_s^2}{a^2}\right)\partial_{1y}(\rho_0 v)\right], \end{aligned} \tag{17b}$$

$$\begin{aligned} A_9+B_9 &= m_9^{(1,eq)} - \left(\frac{2-s_c}{2s_c}\right)\delta_t\left[\frac{1}{3a}\partial_{1x} m_7^{(0,eq)} + \frac{a}{3}\partial_{1y} m_5^{(0,eq)}\right] \\ &- \left(\frac{2-s_c}{2s_c}\right)\delta_t\left[\frac{2c^2}{3a}\partial_{1x}(\rho_0 v) + \frac{2c^2a}{3}\partial_{1y}(\rho_0 u)\right]. \end{aligned} \tag{17c}$$

Note that in Eq. (17) all the terms on the order of $\mathcal{O}(Ma^3)$ or higher have been eliminated.

Now we shall match the LHS of Eq. (16) with the corresponding right-hand side (RHS) of Eq. (17), to determine the unknown equilibrium moments. There are five unknown moments in Eq. (17), namely, $m_2^{(1,eq)}$, $m_5^{(0,eq)}$, $m_7^{(0,eq)}$, $m_8^{(1,eq)}$, and $m_9^{(1,eq)}$.

As a first step, we combine Eq. (16c) with Eq. (17c) to obtain

$$\begin{aligned} -\nu\left[\partial_y(\rho_0 u) + \partial_x(\rho_0 v)\right] &= a\epsilon m_9^{(1,eq)} - a\left(\frac{2-s_c}{2s_c}\right)\delta_t\left[\frac{1}{3a}\partial_x m_7^{(0,eq)} + \frac{a}{3}\partial_y m_5^{(0,eq)}\right] \\ &- a\left(\frac{2-s_c}{2s_c}\right)\delta_t\left[\frac{2c^2}{3a}\partial_x(\rho_0 v) + \frac{2c^2a}{3}\partial_y(\rho_0 u)\right]. \end{aligned} \tag{18}$$

Since the known terms in Eq. (18) only contain the cross velocity gradients, it is natural to set

$$m_5^{(0,eq)} = a_1 c^2 \rho_0 u, \quad m_7^{(0,eq)} = a_2 c^2 \rho_0 v, \tag{19}$$

where a_1 and a_2 are dimensionless constants to be determined. On the LHS of Eq. (18) the coefficients for the two cross velocity gradients are equal. Due to the presence of the term $a\epsilon m_9^{(1,eq)}$, there are multiple possibilities to design $m_5^{(0,eq)}$ and $m_7^{(0,eq)}$. For convenience, we assume $m_9^{(1,eq)}$ is proportional to $c^2\left[\partial_y(\rho_0 u) + \partial_x(\rho_0 v)\right]$, which leads to the following relationship between a_1 and a_2:

$$a_1 = \frac{a_2 - 2r_4}{a^2}. \tag{20}$$

Following the same notation as in [28,29], we set $a_2 = \dfrac{\gamma}{2}$. Then the two moments $m_5^{(0,eq)}$ and $m_7^{(0,eq)}$ can now be written as

$$m_5^{(0,eq)} = \frac{\gamma - r_4}{2a^2} c^2 \rho_0 u, \quad m_7^{(0,eq)} = \frac{c^2\gamma}{2}\rho_0 v. \tag{21}$$

Using the above expressions for $m_5^{(0,eq)}$ and $m_7^{(0,eq)}$, Eq. (17) and Eq. (16) can be combined to provide three equations for the remaining three unknown moments

$$\begin{aligned} &\left\{\frac{1}{3r_7}s_e^*\left(5c^2 - 6c_s^2 + \frac{c^2\gamma}{2}\right)\delta_t + \frac{a^2}{3r_7}s_n^*\left[3c^2a^2 - \frac{c^2(\gamma+4)}{2a^2} - \frac{3r_1r_4c_s^2}{a^2}\right]\delta_t - \nu^V - \nu\right\}\partial_x(\rho_0 u) \\ &+ \left\{\frac{1}{3r_7}s_e^*\left(3c^2a^2 + \frac{c^2\gamma}{2} - 6c_s^2 + 2c^2\right)\delta_t + \frac{a^2}{3r_7}s_n^*\left[\frac{(4+\gamma)c^2a^2}{2} - \frac{3r_1r_4c_s^2}{a^2} - 3c^2\right]\delta_t - \nu^V + \nu\right\}\partial_y(\rho_0 v) \\ &= \frac{1}{3r_7}\epsilon m_2^{(1,eq)} + \frac{a^2}{3r_7}\epsilon m_8^{(1,eq)}, \end{aligned} \tag{22}$$

$$\left\{\frac{a^4}{3r_7}s_e^*\left(5c^2-6c_s^2+\frac{c^2\gamma}{2}\right)\delta_t-\frac{a^2}{3r_7}s_n^*\left[3c^2a^2-\frac{c^2(\gamma+4)}{2a^2}-\frac{3r_1r_4c_s^2}{a^2}\right]\delta_t-\nu^V+\nu\right\}\partial_x(\rho_0 u)$$
$$+\left\{\frac{a^4}{3r_7}s_e^*\left(3c^2a^2+\frac{c^2\gamma}{2}-6c_s^2+2c^2\right)\delta_t-\frac{a^2}{3r_7}s_n^*\left[\frac{(4+\gamma)c^2a^2}{2}-\frac{3r_1r_4c_s^2}{a^2}-3c^2\right]\delta_t-\nu^V-\nu\right\}\partial_y(\rho_0 v) \tag{23}$$
$$=\frac{a^4}{3r_7}\epsilon m_2^{(1,eq)}-\frac{a^2}{3r_7}\epsilon m_8^{(1,eq)},$$
$$\left[s_c^*\frac{c^2(\gamma+4)}{6}\delta_t-\nu\right]\left[\partial_y(\rho_0 u)+\partial_x(\rho_0 v)\right]=a\epsilon m_9^{(1,eq)}, \tag{24}$$

where $s_e^*=(2-s_e)/(2s_e)$, $s_n^*=(2-s_n)/(2s_n)$ and $s_c^*=(2-s_c)/(2s_c)$. Two remarks are noteworthy in the above three equations. First, the three unknown moments $m_2^{(1,eq)}$, $m_8^{(1,eq)}$, and $m_9^{(1,eq)}$ are purposely moved to the RHS of each equation, while the LHS in each equation has the form of strain-rate tensor. The balance between the two sides of each equation guarantees the exact reproduction of stress components in the N–S equations. Second, the ϵ factor in certain terms on the LHS of the above three equations have been merged with $\partial_{1\alpha}$ to convert back to ∂_α.

The above equations allow $\epsilon m_2^{(1,eq)}$, $\epsilon m_8^{(1,eq)}$, and $\epsilon m_9^{(1,eq)}$ be specified as

$$\epsilon m_2^{(1,eq)}=\left[x_1\partial_x(\rho_0 u)+x_2\partial_y(\rho_0 v)\right]c^2\delta_t, \tag{25a}$$
$$\epsilon m_8^{(1,eq)}=\left[x_3\partial_x(\rho_0 u)+x_4\partial_y(\rho_0 v)\right]c^2\delta_t, \tag{25b}$$
$$\epsilon m_9^{(1,eq)}=x_5\left[\partial_x(\rho_0 v)+\partial_y(\rho_0 u)\right]c^2\delta_t, \tag{25c}$$

where the coefficients are all dimensionless and can be determined. They are

$$x_1=\frac{1}{2}\left[s_e^*\left(10-12\frac{c_s^2}{c^2}+\gamma\right)-\frac{12\nu^V}{c^2\delta_t}\right], \tag{26a}$$
$$x_2=\frac{1}{2}\left[s_e^*\left(4-12\frac{c_s^2}{c^2}+\gamma+6a^2\right)-\frac{12\nu^V}{c^2\delta_t}\right], \tag{26b}$$
$$x_3=\frac{s_n^*}{2}\left[6a^2-\frac{\gamma+4}{a^2}-\frac{6r_1r_4}{a^2}\frac{c_s^2}{c^2}\right]-\frac{3r_1r_4}{a^2}\frac{\nu^V}{c^2\delta_t}-\frac{3r_7}{a^2}\frac{\nu}{c^2\delta_t}, \tag{26c}$$
$$x_4=\frac{s_n^*}{2}\left[a^2(\gamma+4)-6-\frac{6r_1r_4}{a^2}\frac{c_s^2}{c^2}\right]-\frac{3r_1r_4}{a^2}\frac{\nu^V}{c^2\delta_t}+\frac{3r_7}{a^2}\frac{\nu}{c^2\delta_t}, \tag{26d}$$
$$x_5=s_c^*\frac{\gamma+4}{6a}-\frac{1}{a}\frac{\nu}{c^2\delta_t}. \tag{26e}$$

Eq. (26a) shows that the bulk viscosity ν^V can be written as

$$\nu^V=\left[\frac{1}{12}s_e^*\left(10-12\frac{c_s^2}{c^2}+\gamma\right)-\frac{1}{6}x_1\right]c^2\delta_t, \tag{27}$$

while Eq. (26e) yields an expression for the shear viscosity ν

$$\nu=\left(s_c^*\frac{\gamma+4}{6}-ax_5\right)c^2\delta_t. \tag{28}$$

Therefore, the addition of the two free parameters, x_1 and x_5, allows the two relaxation times be adjusted, independent of the two viscosities. As noted in the Introduction, this feature is quite desirable because it can be used to either enhance the numerical stability or the model flexibility for simulating flows of different Reynolds numbers or even non-Newtonian flows [34–36]. It should also be noted that the present MRT model is more general than the standard BGK LBM, since the bulk and shear viscosities can be changed independently. An augmented bulk viscosity was found useful for suppressing the acoustic waves resulting from the compressible nature of the LBM in previous studies [41,42]. In Zong et al.'s design [29], this feature is not available.

2.3. A summary of the proposed model

So far, by designing our model to reproduce the N–S equations, we have determined, explicitly, 8 leading-order equilibrium moments in $\mathbf{m}^{(0,eq)}$ and 6 higher-order moments in $\epsilon\mathbf{m}^{(1,eq)}$. The other moments are irrelevant to the N–S equations. For the only flexible leading-order moment, we assume that it has the form $m_3^{(0,eq)}=\xi_1c^4\delta\rho+\xi_2c^2\rho_0\left(u^2+v^2\right)$ as in the square D2Q9 model, where ξ_1 and ξ_2 are free parameters. For the irrelevant terms in $\epsilon\mathbf{m}^{(1,eq)}$, namely, $\epsilon m_3^{(1,eq)}$, $\epsilon m_5^{(1,eq)}$,

and $\epsilon m_7^{(1,eq)}$, we can set them to 0 for simplicity. To summarize, the equilibrium moments derived from the inverse design process in the present model can be expressed as

$$\begin{aligned}\mathbf{m}^{(eq)} &= \mathbf{m}^{(0,eq)} + \epsilon\mathbf{m}^{(1,eq)} \\ &= \begin{Bmatrix} \delta\rho \\ 2\delta\rho(3c_s^2 - r_1c^2) + 3\rho_0(u^2+v^2) \\ \xi_1c^4\delta\rho + \xi_2c^2\rho_0(u^2+v^2) \\ \rho_0 u \\ \dfrac{c^2\rho_0(\gamma - 4r_4)u}{2a^2} \\ \rho_0 v \\ \dfrac{c^2\rho_0\gamma v}{2} \\ \dfrac{r_4}{a^2}(3r_1c_s^2 - 2c^2a^2)\delta\rho + 3\rho_0(a^2u^2 - \dfrac{v^2}{a^2}) \\ \dfrac{\rho_0 uv}{a} \end{Bmatrix} + \begin{Bmatrix} 0 \\ \left[x_1\partial_x(\rho_0 u) + x_2\partial_y(\rho_0 v)\right]c^2\delta_t \\ 0 \\ 0 \\ 0 \\ 0 \\ 0 \\ \left[x_3\partial_x(\rho_0 u) + x_4\partial_y(\rho_0 v)\right]c^2\delta_t \\ x_5\left[\partial_x(\rho_0 v) + \partial_y(\rho_0 u)\right]c^2\delta_t \end{Bmatrix},\end{aligned} \tag{29}$$

where the hydrodynamic variables $\delta\rho$, $\rho_0 u$ and $\rho_0 v$ are obtained as in the standard MRT models as

$$\delta\rho = \sum_i f_i, \qquad \rho_0 u = \sum_i f_i e_{ix}, \qquad \rho_0 v = \sum_i f_i e_{iy}.$$

In the standard MRT-LBM on a square lattice, the equilibrium moments are only functions of conserved quantities, *i.e.*, density and momentum. However, in the present model, the equilibrium moments contain $\epsilon\mathbf{m}^{(1,eq)}$ that are functions of the strain rate tensor, *i.e.*, $\partial_x u$, $\partial_y v$ and $(\partial_x v + \partial_y u)$. The moment equations obtained from the Chapman–Enskog analysis reveal that the strain rate can be calculated as

$$\partial_x u = \frac{c_4 s_e \epsilon m_2^{(1)} - c_2 s_n \epsilon m_8^{(1)}}{\rho_0 (c_1c_4 - c_2c_3) c^2\delta_t}, \tag{30a}$$

$$\partial_y v = \frac{c_3 s_e \epsilon m_2^{(1)} - c_1 s_n \epsilon m_8^{(1)}}{\rho_0 (c_2c_3 - c_1c_4) c^2\delta_t}, \tag{30b}$$

$$(\partial_x v + \partial_y u) = \frac{s_c \epsilon m_9^{(1)}}{\rho_0 c_5 c^2\delta_t}, \tag{30c}$$

where $\epsilon m_i^{(1)} = m_i - m_i^{(0)} = m - m_i^{(0,eq)}$, and

$$c_1 = \left(s_e x_1 - 5 + \frac{6c_s^2}{c^2} - \frac{\gamma}{2}\right), \tag{31a}$$

$$c_2 = \left(s_e x_2 - 3a^2 - \frac{\gamma}{2} + \frac{6c_s^2}{c^2} - 2\right), \tag{31b}$$

$$c_3 = \left[s_n x_3 - 3a^2 + \frac{(\gamma+4)}{2a^2} + \frac{3r_1 r_4}{a^2}\frac{c_s^2}{c^2}\right], \tag{31c}$$

$$c_4 = \left[s_n x_4 - \frac{(\gamma+4)a^2}{a} + \frac{3r_1 r_4}{a^2}\frac{c_s^2}{c^2} + 3\right], \tag{31d}$$

$$c_5 = \left[s_c x_5 - \frac{(\gamma+4)}{6a}\right]. \tag{31e}$$

As implied by Eq. (30c), the assumption we made about the form of $m_9^{(1,eq)}$ previously leads to an explicit and fully mesoscopic expression for the shear strain rate. Therefore, while we introduce $\epsilon\mathbf{m}^{(1,eq)}$ into our model, the model remains fully mesoscopic, and the collision is still local.

3. General guidelines for setting adjustable parameters in the proposed model

For the proposed model, we may conclude from Eq. (26) and (29) that all the parameters are functions of two model parameters (γ and c_s^2), three relaxation parameters (s_e, s_n and s_c), and two other free parameters (ξ_1 and ξ_2). The other four relaxation parameters, *i.e.*, s_ρ, s_j, s_ε and s_q are irrelevant to the N–S equations, so we can set their values arbitrarily. Without any external forcing, the usual practice is to set the two relaxation parameters of conserved moments (s_ρ and s_j)

to 0, while the other two are specified for better numerical stability. Before presenting the numerical validation results of our proposed model, it is important to address how to specify all these parameters, especially the newly introduced ones.

First, the two free parameters ξ_1 and ξ_2 have no effect on the N–S equations and thus they may be chosen arbitrarily. A common (but not necessarily the best) choice is to set $\xi_1 = 1$ and $\xi_2 = -3$ so the energy square moment is consistent to the equilibrium distribution in the standard D2Q9 lattice BGK model. Next, for the model parameter γ, we realize that when $a = 1$, it must recover its value of -2 as in the standard MRT model. Using this value as a baseline, we suggest that γ be chosen in the range of $-4 < \gamma < 0$. This ensures that the first term on the RHS of Eq. (28) is maintained positive since the viscosity should always be positive in the absence of the additional term involving x_5. When the aspect ratio a changes, the variation of γ can be qualitatively described from the knowledge of kinetic theory. When $a < 1$, the lattice velocity in y direction is reduced, leading to a smaller overall diffusivity due to the smaller molecular mean-free-path. At the macroscopic level, the reduction of diffusivity implies a smaller shear viscosity. Therefore, the shear viscosity needs to be lowered as a is decreased. Therefore, from Eq. (28) we may conclude that a smaller γ should be applied for smaller a, and vice versa. This is the guideline for setting γ for different a values used in the simulations to be discussed later.

The speed of sound, c_s, on the other hand, is an intrinsic tunable parameter in the MRT models [38]. It is usually set to $\delta_x/(\sqrt{3}\delta_t)$, to be consistent with the corresponding lattice BGK model. In LBM, the value of c_s affects the valid range of velocity magnitude as local Ma must be kept small. For the proposed rectangular-lattice model, we expect that the value of c_s depends on both δ_x/δ_t and δ_y/δ_t. If we set $\delta_x = 1$, it follows that, as the grid aspect ratio a is increased, c_s is likely increased. On the other hand, the value for c_s may be reduced for a smaller a. This inherent dependence of c_s on a implies that the valid velocity magnitudes in the rectangular lattice model would also depend on the value of a.

Finally, we need to specify the three key relaxation parameters in the present model. Once γ is chosen and the physical shear viscosity ν is known, s_c can be determined from Eq. (28). In order to maintain a good stability of the model, we can always set s_c close to one, regardless of the physical shear viscosity, due to the inclusion of the parameter x_5 in Eq. (28).

In the previous designs of MRT-LB models on a rectangular lattice [28,29], the following relationships are derived as partial requirements for isotropy of the viscosity coefficients:

$$s_e^* = \frac{2(\gamma+4)\left[\left(\frac{12c_s^2}{c^2}-\gamma\right)r_1 - 2\left(5a^2+1\right)\right]}{r_1\left(\gamma+1-3a^2\right)\left(\gamma+10-\frac{12c_s^2}{c^2}\right)+6\left[a^4(\gamma-2)-3r_4\right]}s_c^*, \tag{32a}$$

$$s_n^* = \frac{2(\gamma+4)\left[\left(\frac{12c_s^2}{c^2}-\gamma\right)r_1 - 2\left(3a^4+5r_1\right)\right]}{r_1\left(\gamma+1-3a^2\right)\left(\gamma+10-\frac{12c_s^2}{c^2}\right)+6\left[a^4(\gamma-2)-3r_4\right]}s_c^*. \tag{32b}$$

However, in the present model, due to the introduction of $\epsilon\mathbf{m}^{(1,eq)}$ and the five additional degrees of freedom x_1 to x_5, the above two relationships are not necessary and one is encouraged to fully explore the different choices of relaxation parameters. In the numerical validations to be presented in Sec. 4, for the purpose of fair comparisons between results from the present model and Bouzidi et al.'s model, the above relations are still used unless indicated otherwise.

4. Numerical validations

In order to validate the present model, two different flows will be considered: an unsteady 2D decaying Taylor–Green vortex flow and a steady lid-driven cavity flow. The simulation results from the present models are compared to theoretical results or other numerical results. Since the present model is an improvement over Bouzidi et al.'s model, we also compare results from our model to those based on Bouzidi et al.'s model.

4.1. The decaying Taylor–Green vortex flow

The 2D decaying Taylor–Green vortex flow is an array of periodic vortices that maintain their structure with the velocity magnitude decaying in time due to the viscous dissipation. The flow is governed by the incompressible N–S equations. In a physical domain of $(x, y) \in (0 : L_x, 0 : L_y)$ with periodic boundary conditions in both spatial directions, the flow is described by the time-dependent analytical solution

$$u(x, y, t) = -U_0 \cos(k_x x)\sin(k_y y)\, e^{-k^2\nu t}, \tag{33a}$$

$$v(x, y, t) = \frac{k_x}{k_y} U_0 \sin(k_x x)\cos(k_y y)\, e^{-k^2\nu t}, \tag{33b}$$

$$p(x, y, t) = -\frac{1}{4}\rho_0 U_0^2 \left[\cos(2k_x x) + \left(\frac{k_x}{k_y}\right)^2 \cos(2k_y y)\right] e^{-2k^2\nu t} + P_0, \tag{33c}$$

where U_0 is the initial velocity magnitude, ν is the kinetic viscosity, $k_x = 2\pi/L_x$ and $k_y = 2\pi/L_y$ are the wave numbers in x and y directions, respectively, $k = \sqrt{k_x^2 + k_y^2}$, and P_0 is a constant background pressure, which can take an arbitrary value. We consider a square domain with $L_x = L_y = L$, the solution becomes

$$u(x, y, t) = -U_0 \cos\left(\frac{2\pi x}{L}\right) \sin\left(\frac{2\pi y}{L}\right) e^{-\frac{8\pi^2 \nu t}{L^2}}, \tag{34a}$$

$$v(x, y, t) = U_0 \sin\left(\frac{2\pi x}{L}\right) \cos\left(\frac{2\pi y}{L}\right) e^{-\frac{8\pi^2 \nu t}{L^2}}, \tag{34b}$$

$$p(x, y, t) = -\frac{1}{2}\rho_0 U_0^2 \cos\left[\frac{2\pi}{L}(x - y)\right] \cos\left[\frac{2\pi}{L}(x + y)\right] e^{-\frac{16\pi^2 \nu t}{L^2}} + P_0, \tag{34c}$$

which leads to expressions of normal and shear stress τ_{xx}, τ_{yy}, and τ_{xy} as

$$\tau_{xx} = \rho_0 \nu \left(\partial_x u - \partial_y v\right) = \frac{4\pi \rho_0 \nu U_0}{L} \sin\left(\frac{2\pi x}{L}\right) \sin\left(\frac{2\pi y}{L}\right) e^{-\frac{8\pi^2 \nu t}{L^2}}, \tag{35a}$$

$$\tau_{yy} = -\tau_{xx} = -\frac{4\pi \rho_0 \nu U_0}{L} \sin\left(\frac{2\pi x}{L}\right) \sin\left(\frac{2\pi y}{L}\right) e^{-\frac{8\pi^2 \nu t}{L^2}}, \tag{35b}$$

$$\tau_{xy} = \rho_0 \nu \left(\partial_x v + \partial_y u\right) = 0. \tag{35c}$$

Since this is an unsteady flow, a consistent mesoscopic initial condition is essential [43]. Such an initial condition specifies not only the velocity field, but also the initial pressure and stress fields. For the Taylor–Green flow, there are two different methods to configure the initial distribution functions. The first method is to use the moment equations resulting from the first-order Chapman–Enskog analysis, namely, Eq. (10b), to specify the initial $\epsilon m_i^{(1)}$, as

$$\epsilon m_1^{(1)} = \epsilon m_4^{(1)} = \epsilon m_6^{(1)} = 0, \tag{36a}$$

$$\epsilon m_2^{(1)} = \rho_0 \frac{\delta_t}{s_e}\left[\left(\frac{s_e x_1}{\delta_t} - 5 + 6c_s^2 - \frac{\gamma}{2}\right)\partial_x u + \left(\frac{s_e x_2}{\delta_t} - 3a^2 - \frac{\gamma}{2} + 6c_s^2 - 2\right)\partial_y v\right], \tag{36b}$$

$$\epsilon m_3^{(1)} = -\rho_0 \frac{\delta_t}{s_\varepsilon}\left[\frac{(\gamma + 4 - 4a^2)}{2a^2}\partial_x u + \frac{\gamma}{2}\partial_y v\right], \tag{36c}$$

$$\begin{aligned}\epsilon m_5^{(1)} = &-\rho_0 \frac{\delta_t}{s_q}\left[\left(\frac{6a^2 - \gamma - 4}{2a^2}\right)\left(u\partial_y v + v\partial_x u\right) + \left(\frac{\xi_1 - 4}{3c_s^2} + \frac{4a^2 - \gamma}{2a^2}\right)\frac{\partial_x p}{\rho_0}\right] \\ &- \rho_0 \frac{\delta_t}{s_q}\left[2u\left(\frac{\xi_2}{3} - \frac{\gamma - 4r_4}{2a^2}\right)\partial_x u + 2v\left(\frac{\xi_2}{3} + \frac{2}{a^2}\right)\partial_x v\right],\end{aligned} \tag{36d}$$

$$\begin{aligned}\epsilon m_7^{(1)} = &-\rho_0 \frac{\delta_t}{s_q}\left\{\left(1 - \frac{\gamma}{2}\right)\left(u\partial_y v + v\partial_x u\right) + \left[2a^2 + \frac{a^2(\xi_1 - 4)}{3c_s^2} - \frac{\gamma}{2}\right]\frac{\partial_y p}{\rho_0}\right\} \\ &- \rho_0 \frac{\delta_t}{s_q}\left[2a^2 u\left(\frac{\xi_2}{3} + 2\right)\partial_y u + 2v\left(\frac{a^2 \xi_2}{3} - \frac{\gamma}{2}\right)\partial_y v\right],\end{aligned} \tag{36e}$$

$$\begin{aligned}\epsilon m_8^{(1)} = &\rho_0 \frac{\delta_t}{s_n}\left[\frac{s_n x_3}{\delta_t} - 3a^2 + \frac{(\gamma + 4)}{2a^2} + \frac{3r_1 r_4 c_s^2}{a^2}\right]\partial_x u \\ &+ \rho_0 \frac{\delta_t}{s_n}\left[\frac{s_n x_4}{\delta_t} + 3 + \frac{a^2(\gamma + 4)}{2} + \frac{3r_1 r_4 c_s^2}{a^2}\right]\partial_y v,\end{aligned} \tag{36f}$$

$$\epsilon m_9^{(1)} = \rho_0 \frac{\delta_t}{s_c}\left[\frac{s_c x_5}{\delta_t} - \frac{(\gamma + 4)}{6a}\right]\left(\partial_x v + \partial_y u\right). \tag{36g}$$

Combine $\epsilon m_i^{(1)}$ with the leading-order $m_i^{(0)} = m_i^{(0,eq)}(\delta\rho, u, v)$, we obtain an adequate approximation of all initial moments. They can be transformed to determine the initial distribution functions by $\mathbf{f} = \mathbf{M}^{-1}\left(\mathbf{m}^{(0)} + \epsilon\mathbf{m}^{(1)}\right)$. The second method is to apply the iterative method similar to the one introduced in [43]. Since the initial pressure field is well defined, the purpose of the iteration is to only converge the distribution functions to yield the correct stress fields. The iteration is performed as follows:

1. Begin by setting $\mathbf{m}(\mathbf{x}, t = 0) = \mathbf{m}^{(0,eq)}[\delta\rho(\mathbf{x}, t = 0), u(\mathbf{x}, t = 0), v(\mathbf{x}, t = 0)]$.
2. Perform the collision step and then streaming step.
3. Calculate moments $\mathbf{m}$ after the streaming step, but replace $\delta\rho$, j_x, and j_y by their initial solutions.

Table 1
The model parameters and simulation setting for the decaying Taylor–Green vortex flow.

Case #	a	$n_x \times n_y$	U_0	ν	ν^V	γ
1	4.0	200×50	0.1	0.2	0.3158	−0.2
2	2.0	200×100	0.125	0.25	0.0603	−1.6
3	0.5	200×400	0.05	0.1	0.0323	−2.9
4	0.25	200×800	0.016	0.032	0.032	−3.95
Case #	c_s^2	s_e	s_n	s_c	x_1	x_5
1	0.4	1.2258	0.9923	1.2258	−1.1053	0.0
2	0.4	1.7938	0.956	0.8889	−0.2586	0.0
3	0.15	1.5943	0.5194	0.9565	0.1432	0.0
4	0.03	1.000	1.5725	1.000	1.2305	−0.1113

4. Calculate the normal and shear stress components, if they are converged as

$$\max\left[\left|\frac{\tau_{xx}(i,j,\delta t)-\tau_{xx}(i,j,t=0)}{4\pi\nu\rho_0 U_0/L}\right|\right]<\zeta,\quad \max\left[\left|\frac{\tau_{xy}(i,j,\delta t)-\tau_{xy}(i,j,t=0)}{4\pi\nu\rho_0 U_0/L}\right|\right]<\zeta, \tag{37}$$

where i, j are grid indices, ζ is a small threshold value and is set to 10^{-9}, the initialization is done. Otherwise, update $\tau_{xx}(i,j,t=0)$ and $\tau_{xy}(i,j,t=0)$ with $\tau_{xx}(i,j,\delta_t)$ and $\tau_{xy}(i,j,\delta_t)$, respectively, and repeat Step 2 to Step 4.

According to our tests, the two initialization methods yield the same consistent results of the initial distribution functions. In the following tests, only the first method is applied.

The initial flow Reynolds number $Re = U_0 L/\nu$ is set to 100. The present model is tested with different values of the grid aspect ratio a. The model parameters for different cases are presented in Table 1. Of significance is to observe the sensitive dependence of γ and c_s on a, as discussed in Sec. 3. Consequently, the velocity magnitude U_0 and the shear viscosity ν must also depend on a. For Case 1 and Case 4, the relationship between s_e and s_c, Eq. (32a), is not used, due to otherwise the extreme value of s_e we would obtain. The parameter x_1 and x_5 are used to enhance the numerical stability, by keeping both s_e and s_c close to one.

First, we present the velocity and pressure profiles along a vertical line at $x = 0.1475L$ across the whole domain at the normalized time $t\nu/L^2 = 0.005$ in Fig. 2. The location $x = 0.1475L$ is chosen for comparison as both velocity and pressure at this position have non-trivial values and no interpolation is needed (this position coincides with a grid mesh line). Fig. 2 shows that both the present model and Bouzidi et al.'s model yield accurate velocity profiles that are in excellent agreement with the theoretical solution. However, the pressure profiles obtained from Bouzidi et al.'s model deviate from the theoretical solution significantly, while the pressure profiles from the present model still match the theoretical benchmark, with only very minor differences. The very minor errors in the present model are due to insufficient resolutions in y directions when a large a value is used, as well as the influence of the acoustic waves which will be addressed in detail later. The large deviations in the results from Bouzidi et al.'s model, however, mainly result from the anisotropic viscosities in the two directions.

To further reveal the level of errors in different models, the time evolutions of pressure and pressure gradient at two locations $(x, y) = (0.15L, 0.2L)$ and $(0.15L, 0.3L)$ will be discussed next. Again, two locations chosen for probing are based on the lattice nodes so no interpolation is needed. In different cases, because the boundary lattice nodes are always half lattice distance away from the physical boundary, the physical locations will be slightly different for different grid resolutions. Therefore, we do not compare the results between different resolutions. Only the results from Case 3 and Case 4 are presented. The time evolutions of pressure p, pressure gradient $\partial_x p$ and $\partial_y p$ are shown in Fig. 3, 4, and 5, respectively.

Figs. 3 to 5 clearly illustrate the discrepancy between the pressure results of Bouzidi et al.'s model and the corresponding theoretical solutions. The results from the present model, on the other hand, agree well with the theoretical benchmarks. Due to the anisotropic viscosities in Bouzidi et al.'s model, the velocity components in x and y directions decay at different rates. However, the continuity equation is still satisfied, which corrects the different decaying rates through the pressure redistribution. Unfortunately, the exchange in the two directions by pressure does not fully remove the anisotropic decay rates, and this dynamics causes significant oscillations in the local pressure. Such oscillations are not caused by the acoustic waves since they always appear on one side of the corresponding theoretical results. On the other hand, the much smaller oscillations in the results of the present model are related to the acoustic waves, such minor pressure oscillations had also been observed in the previous studies, for example, the bottom-left plots of Fig. 1 and Fig. 2 in [43], and confirmed by our own test results from the standard MRT model with the same physical settings in Fig. 6.

Fig. 7 displays the normal stress profiles across the same vertical line at the same time as in Fig. 2. In order to examine the isotropy of both our model and Bouzidi et al.'s model, we defined ν_x and ν_y as the shear viscosities associated with the normal stress components in the resulting hydrodynamic equations in the x- and y-directions, respectively, following the definitions by Zong et al. [29]. The theoretical results for Bouzidi et al.'s model are provided in [29], which, in our notation, can be stated as

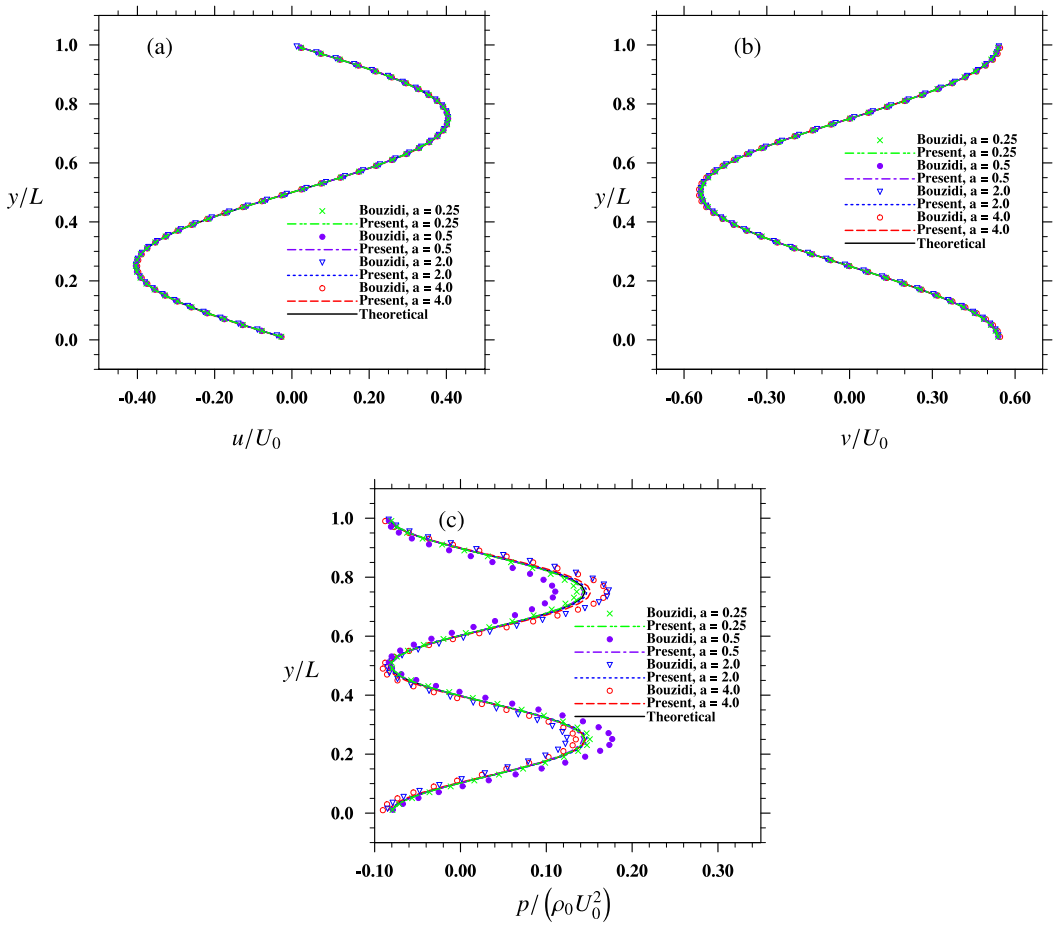

Fig. 2. The profiles of conserved moments along the vertical line at $x = 0.1475L$ through the flow domain: (a) normalized u, (b) normalized v, (c) normalized p.

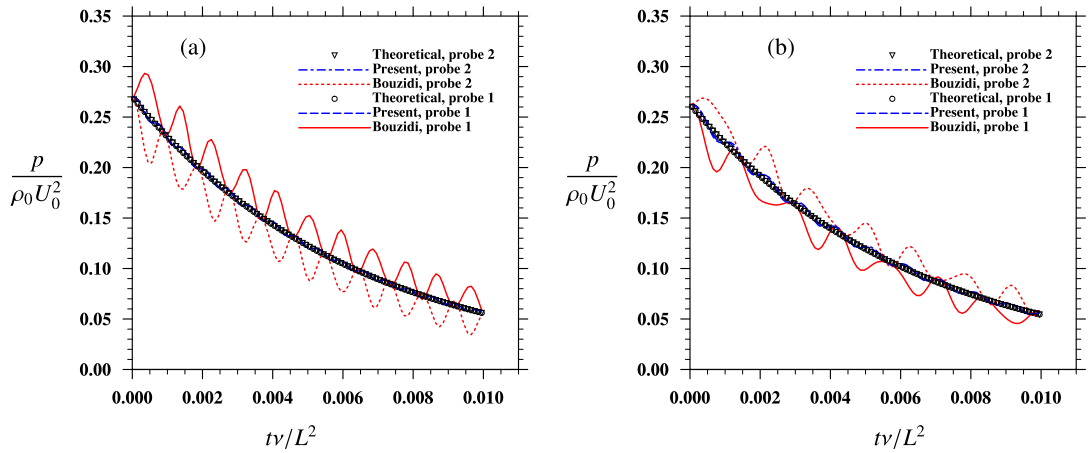

Fig. 3. The time evolution of pressure at two selected locations. Probe 1 is at location $(0.15L, 0.2L)$ and probe 2 at $(0.15L, 0.3L)$. (a) $a = 0.5$, (b) $a = 2.0$.

$$\nu_x^B = \left[-\frac{r_4 s_e^*}{2r_7} + \frac{s_n^*}{12r_7}\left(2r_7 + 6r_4 - r_7\gamma\right)\right]c^2\delta_t, \tag{38a}$$

$$\nu_y^B = \left[\frac{a^4 r_4 s_e^*}{2r_7} + \frac{s_n^*}{12r_7}\left(2r_7 + 6r_4 - r_7\gamma\right)\right]c^2\delta_t. \tag{38b}$$

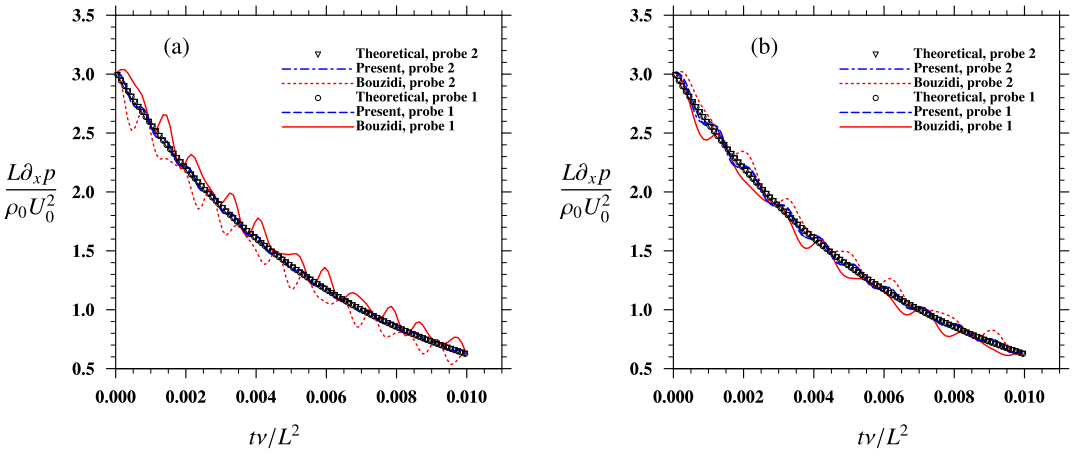

Fig. 4. The time evolution of pressure gradient $\partial_x p$ at two selected locations. Probe 1 is at location $(0.15L, 0.2L)$ and probe 2 at $(0.15L, 0.3L)$. (a) $a = 0.5$, (b) $a = 2.0$.

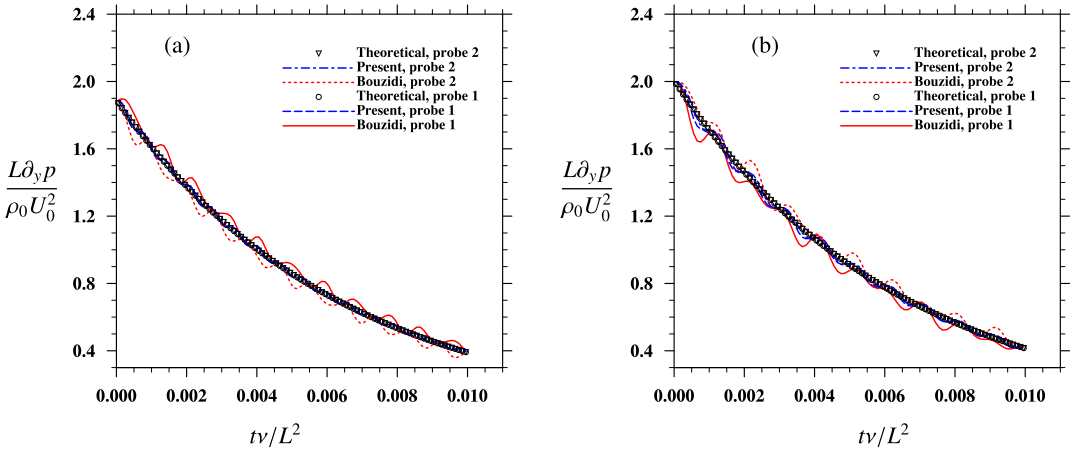

Fig. 5. The time evolution of pressure gradient $\partial_y p$ at two selected locations. Probe 1 is at location $(0.15L, 0.2L)$ and probe 2 at $(0.15L, 0.3L)$. (a) $a = 0.5$, (b) $a = 2.0$.

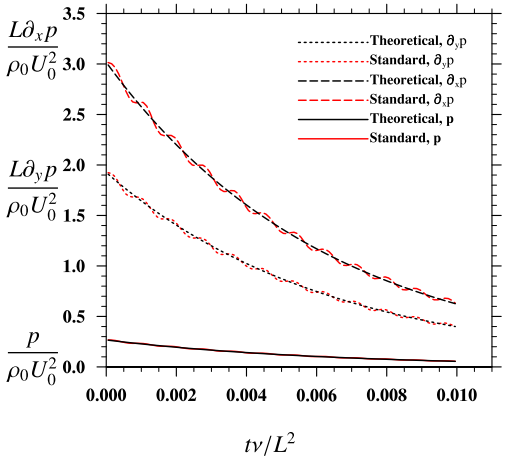

Fig. 6. The time evolution of pressure and pressure gradients at a point $(0.15L, 0.2L)$ from the standard MRT model on a square lattice.

Table 2
The model viscosity coefficients for the cases considered for the decaying Taylor–Green vortex flow.

Case #	ν_x^B	ν_y^B	ν_x^P	ν_y^P	ν
1	0.1072	0.2928	0.2	0.2	0.2
2	0.2069	0.2931	0.25	0.25	0.25
3	0.1239	0.0761	0.1	0.1	0.1
4	0.0338	0.0302	0.032	0.032	0.032

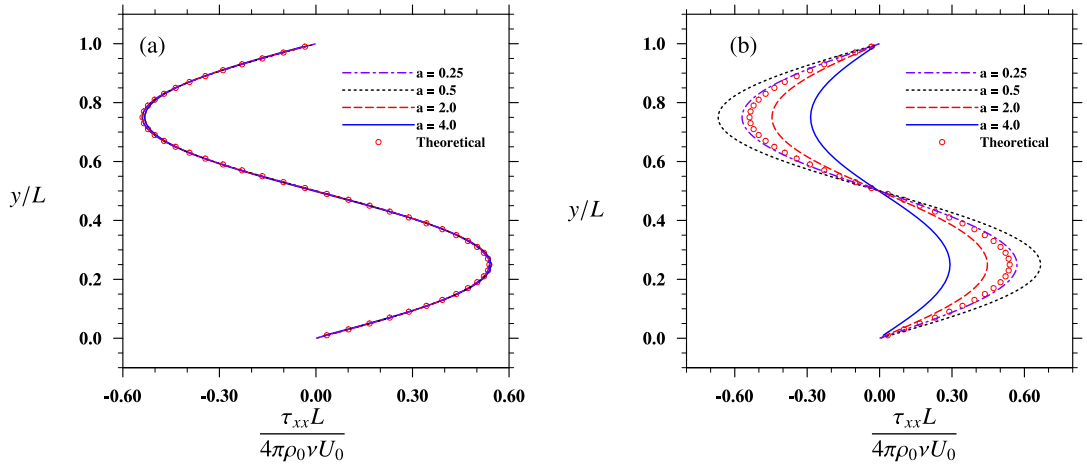

Fig. 7. The normal stress profiles on a vertical line at $x = 0.1475L$ and $t\nu/L^2 = 0.005$: (a) the present model, (b) Bouzidi et al.'s model.

While for the present model, they are derived from Eq. (22) and Eq. (23), as

$$\nu_x^P = \left[-\frac{r_4 s_e^*}{2r_7} + \frac{s_n^*}{12r_7}(2r_7 + 6r_4 - r_7\gamma) - \frac{(x_1 - x_2)}{6r_7} - \frac{a^2(x_3 - x_4)}{6r_7}\right]c^2\delta_t, \tag{39a}$$

$$\nu_y^P = \left[\frac{a^4 r_4 s_e^*}{2r_7} + \frac{s_n^*}{12r_7}(2r_7 + 6r_4 - r_7\gamma) + \frac{a^4(x_1 - x_2)}{6r_7} - \frac{a^2(x_3 - x_4)}{6r_7}\right]c^2\delta_t. \tag{39b}$$

Since the second terms of Eq. (38a) and Eq. (38b) are identical, for Bouzidi et al.'s model, the only case that the fully isotropy, $\nu_x^B = \nu_y^B$, can be restored is when $a = 1$, *i.e.*, in the square lattice. It is also noteworthy that the present model can be reduced to Bouzidi et al.'s model by having $x_1 = x_2$ and $x_3 = x_4$. For all cases in Table 1, we listed these directional viscosity values in Table 2. It is clear from the results that Bouzidi et al.'s model fails to satisfy this isotropy condition.

Due to this lack of isotropy, the normal stress profiles from Bouzidi et al.'s model also deviate significantly from the theoretical solutions, which can be clearly observed in Fig. 7(b). The level of errors corresponds precisely to the level of relative difference between ν_x and ν_y in Table 2, namely, Case 1 is the worst case. The normal stress profiles calculated from the present model, on the other hand, are all in excellent agreement with the theory, except a very minor error for Case 1 ($a = 4.0$) which could result from the insufficient resolution in that case.

Finally, we examine the time evolution of the ratio of the average kinetic energy in the x direction to that in the y direction, for different grid aspect ratios (Fig. 8). Theoretically, the average kinetic energy in the two directions can be evaluated as

$$\bar{E}_x = \frac{1}{2}\left\langle u^2(x, y, t)\right\rangle = \bar{E}_y = \frac{1}{2}\left\langle v^2(x, y, t)\right\rangle = \frac{1}{8}U_0^2 e^{-2k^2\nu t}. \tag{40}$$

Thus the theoretical ratio is one at all times. As shown in Fig. 8, for Bouzidi et al.'s model, the ratios obtained from different a values deviate much more significantly from 1, when compared to results from the present model. The minor oscillations in the present model are related to the acoustic waves as indicated earlier.

So far, through benchmarking the results related to the pressure, the normal stress, and energy decaying rate, we have confirmed the isotropy of viscosity coefficients in the present model. The next question of concern is whether the model can preserve the second order accuracy of the regular MRT-LB models. Comparing to the regular MRT-LB models, the only difference in the present model is the addition of strain-rate components in $\epsilon\mathbf{m}^{(1,eq)}$. As the strain rate tensor is obtained mesoscopically, we expect that the second-order accuracy is preserved [44].

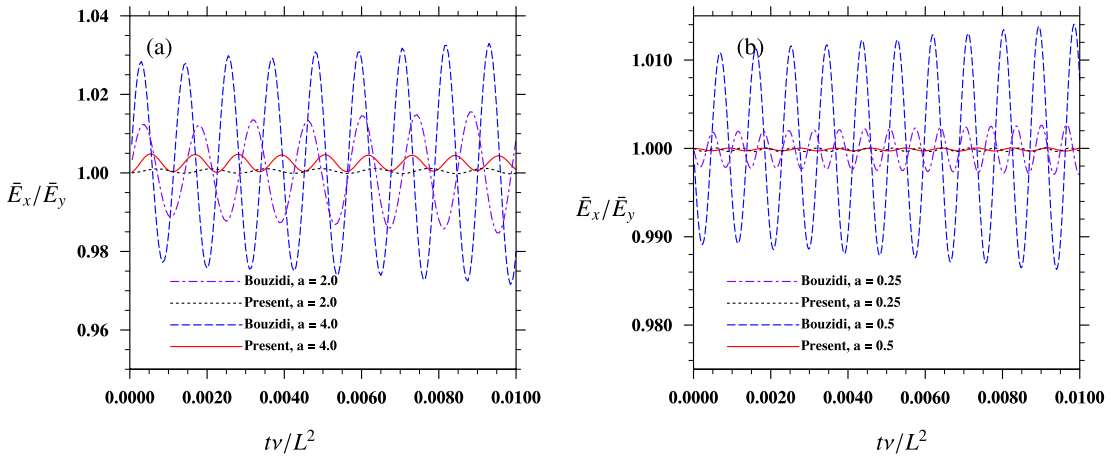

Fig. 8. The ratio of averaged kinetic energy in the x direction to that in the y direction: (a) Case 1 and 2; (b) Case 3 and 4.

Table 3
The L1 and L2 error norms and the order of accuracy for the velocity and normal stress at half-life time, for $a = 2.0$.

$n_x \times n_y$	$\mathbf{u}\,(L1)$	order	$\mathbf{u}\,(L2)$	order	$\tau_{xx}\,(L2)$	order	$\tau_{xx}\,(L2)$	order
50×25	5.9555E−3	(−)	1.8769E−2	(−)	6.6101E−3	(−)	6.0545E−3	(−)
100×50	1.5863E−3	1.91	6.4678E−3	1.54	1.7869E−3	1.89	1.6247E−3	1.90
200×100	3.5561E−4	2.16	2.2513E−3	1.52	3.9487E−4	2.18	3.6011E−4	2.17
400×200	1.0020E−4	1.83	7.9386E−4	1.50	1.0154E−4	1.96	9.2616E−5	1.96
Overall		1.96		1.52		2.01		2.01

Table 4
The L1 and L2 error norms and the order of accuracy for the velocity and normal stress at half-life time, for $a = 0.5$.

$n_x \times n_y$	$\mathbf{u}\,(L1)$	order	$\mathbf{u}\,(L2)$	order	$\tau_{xx}\,(L2)$	order	$\tau_{xx}\,(L2)$	order
25×50	4.0963E−3	(−)	3.9733E−3	(−)	1.2166E−2	(−)	1.1592E−2	(−)
50×100	1.4699E−3	1.48	1.4612E−3	1.44	3.0278E−3	2.01	2.8681E−3	2.02
100×200	1.2796E−4	3.52	1.2445E−4	3.55	6.7774E−4	2.16	6.4487E−4	2.15
200×400	8.1722E−5	0.65	8.0761E−5	0.62	1.8772E−4	1.85	1.7777E−4	1.86
Overall		1.88		1.87		2.01		2.01

To confirm this, for different a values, we simulate the Taylor–Green flow with different grid resolutions and calculate the L1 and L2 error norms using with theoretical solution as the benchmark. The L1 and L2 error norms are defined as

$$\varepsilon_{L1}(t) = \frac{\sum_{x,y} | q_n(x,y,t) - q_t(x,y,t) |}{\sum_{x,y} | q_t(x,y,t) |}, \tag{41a}$$

$$\varepsilon_{L2}(t) = \frac{\sqrt{\sum_{x,y} | q_n(x,y,t) - q_t(x,y,t) |^2}}{\sqrt{\sum_{x,y} | q_t(x,y,t) |^2}}, \tag{41b}$$

where q_n and q_t represent the numerical solution and the theoretical solution, respectively. For each a value, we choose $Re = 10$ and $\nu = \nu^V$ for faster dissipation of the acoustic waves. The other parameters are kept identical to the values in Table 1. The L1 and L2 error norms are calculated at the half-life time of the flow, when the flow velocity magnitude decays to half of the initial value. The results of $a = 2.0$ and $a = 0.5$ are shown in Table 3 and Table 4, respectively.

From these two tables we conclude that almost all the results suggest a roughly second-order convergence for both velocity and stress. The only exception is the L2 norm of velocity in $a = 2.0$ case, which shows a 1.5 order convergence. Generally, due to the effects of acoustic waves, the convergence speed of velocity oscillates around 2. On the other hand, since the normal stress depends less on the leading-order equilibrium moments, the variation of the convergence speed is also expected to be less, as demonstrated by the data in these tables.

4.2. The 2D lid-driven cavity flow

The lid-driven cavity flow has been widely used as a standard benchmark case in many numerical studies [42,45–47]. In this section, we consider the flow driven by the moving lid (lid velocity u_w) over a square cavity where the aspect ratio

Table 5
Model parameters and simulation setting used in the 2D lid-driven cavity flow.

Case #	a	$n_x \times n_y$	u_w	ν	ν^V
1	4.0	400×100	0.05	0.2	0.2
3	2.0	200×100	0.0625	0.125	0.125
3	0.5	200×400	0.05	0.1	0.0323
4	0.25	200×800	0.016	0.032	0.032
Case #	γ	c_s^2	s_e	s_n	s_c
1	−0.2	0.4	1.2258	0.9923	1.2258
3	−1.6	0.4	1.8913	1.2937	1.2308
3	−2.9	0.15	1.5943	0.5194	0.9565
4	−3.95	0.03	1.000	1.5725	1.000

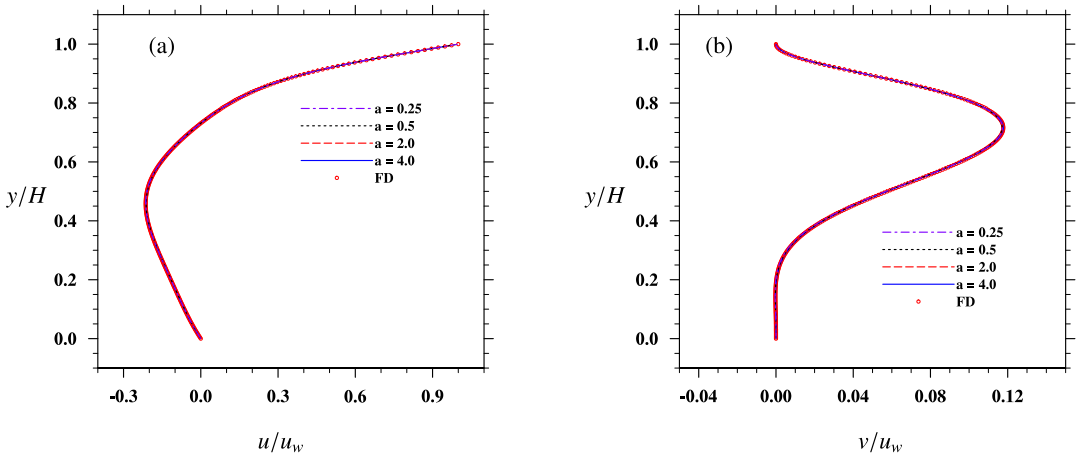

Fig. 9. The velocity profile along the vertical line through the geometric center of cavity: (a) u; (b) v.

of $L/H = 1$, where L and H are the cavity width and height, respectively. To correctly handle the solid–fluid interface, the boundary walls are purposely placed half lattice length from the boundary fluid nodes so the exact mid-link bounce back is naturally conducted. Specially, at the top moving wall, the following bounce back scheme is applied

$$f_{\bar{i}}\left(\mathbf{x}_b, t+\delta_t\right) = \tilde{f}_i\left(\mathbf{x}_b, t\right) + \left[f_{\bar{i}}^{(eq)}\left(\mathbf{u}_w, \delta\rho_w\right) - f_i^{(eq)}\left(\mathbf{u}_w, \delta\rho_w\right)\right], \tag{42}$$

where i is the lattice direction incident to the wall and $\bar{i}$ is its opposite direction, *i.e.*, $\mathbf{e}_{\bar{i}} = -\mathbf{e}_i$, $\tilde{f}_i$ is the distribution after the collision substep, $f_i^{(eq)}\left(\mathbf{u}_w, \delta\rho_w\right)$ and $f_{\bar{i}}^{(eq)}\left(\mathbf{u}_w, \delta\rho_w\right)$ are obtained from the inverse transfer of the equilibrium moments.

With the flow Reynolds number $Re = u_w L/\nu$ fixed at 100, we simulate the cavity flow with different grid aspect ratios, as shown in Table 5. After the flow reaches the steady state, the velocity profiles for different cases along the half channel width $x = L/2$ and half channel height $y = H/2$ are shown in Fig. 9 and Fig. 10, respectively. The benchmark results are obtained from a fractional-step second-order finite-difference scheme [47] on a 256×256 staggered grid. From both figures, we observe that the present model at all aspect ratios produces consistent and accurate results when compared to the finite-difference benchmark results.

We next investigate the normal stress (Fig. 11) and shear stress (Fig. 12) profiles along the same vertical and horizontal lines. The normal stress components τ_{xx} and τ_{yy} are computed from ν_x and ν_y and corresponding normal strain rates, respectively. The shear stress profiles, on the other hand, come directly from Eq. (36g). The corresponding results from Bouzidi et al.'s model are also presented for comparison.

As shown in Fig. 11, all the normal stress profiles from the present model are in excellent agreement with the finite-difference benchmark except the sudden jumps close to the moving lid when the vertical grid resolution is low (*i.e.*, large a). The jumps are due to the pressure kinks that had previously been observed by Luo et al. [42] in cavity flow simulations with the standard MRT-LB model on a square grid. Different from the standard MRT model that can address this issue by using the same relaxation parameters for the energy and normal stress moments, in the present model, due to the fact that such two moments are coupled with each other, there is no simple solution to eliminate the kinks with relatively low resolutions in the vertical direction. However, with the increase of the vertical resolution, the kinks can be effectively reduced, as shown by the results for small a cases. The shear stress profiles, on the other hand, match perfectly with the benchmark results without any jump close to the moving wall. This in a way confirms that the jumps in the normal stress profiles are related to the pressure kinks since the shear stress and pressure moments are decoupled. Bouzidi et al.'s model, however,

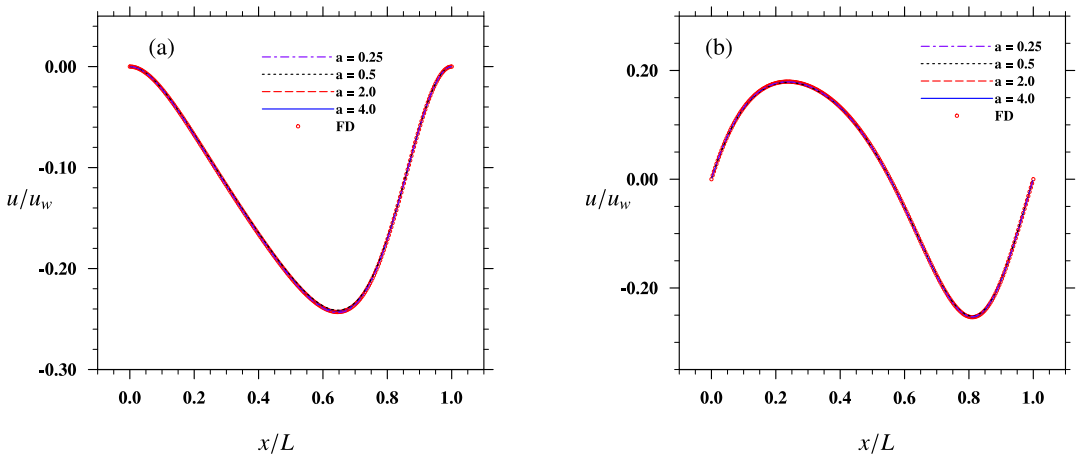

Fig. 10. The velocity profile along the horizontal line through the geometric center of cavity: (a) u; (b) v.

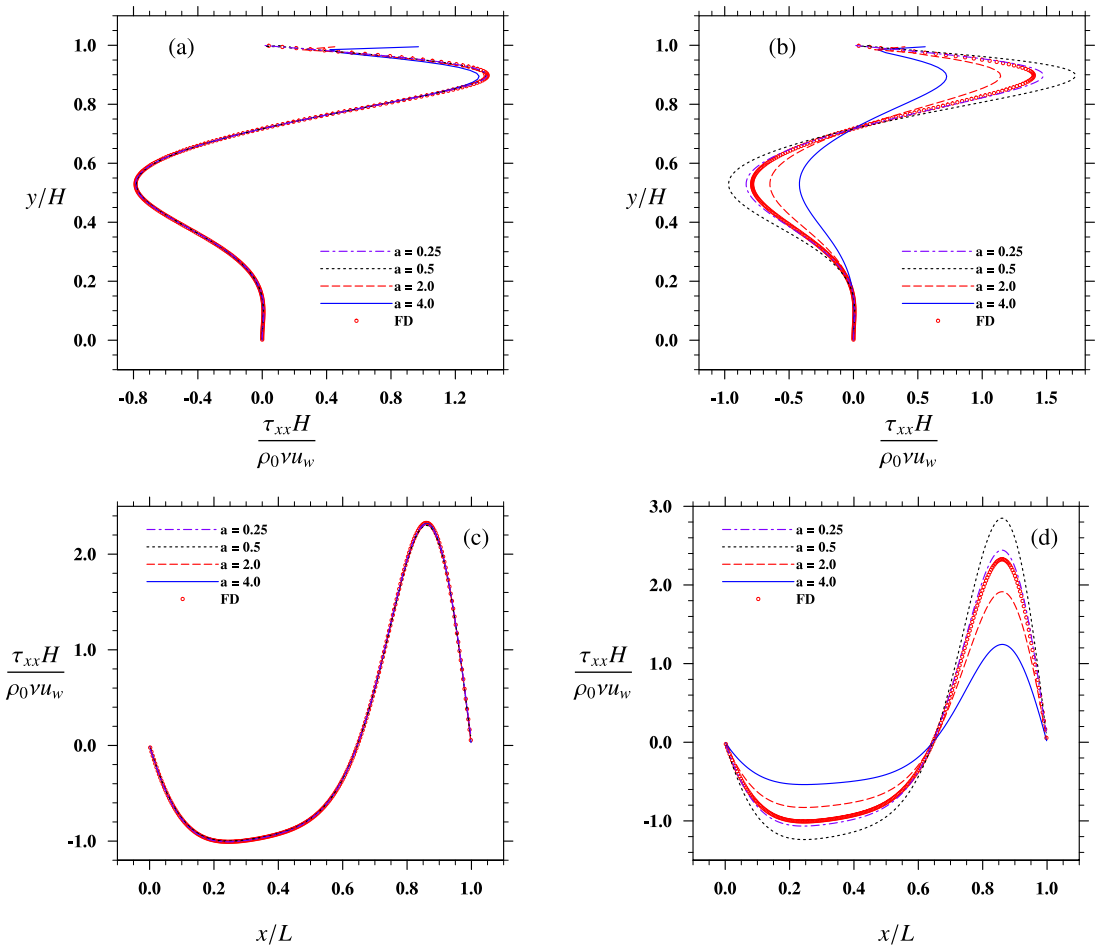

Fig. 11. The normal stress profiles along a vertical line ((a) and (b)) and a horizontal line ((c) and (d)) through the geometric center of cavity: (a), (c) τ_{xx}, the present model; (b), (d) τ_{xx}, Bouzidi et al.'s model.

again fails to provide correct results for the normal stress due to anisotropic viscosity coefficients, although the shear stress results can be correctly simulated when compared to the benchmark results.

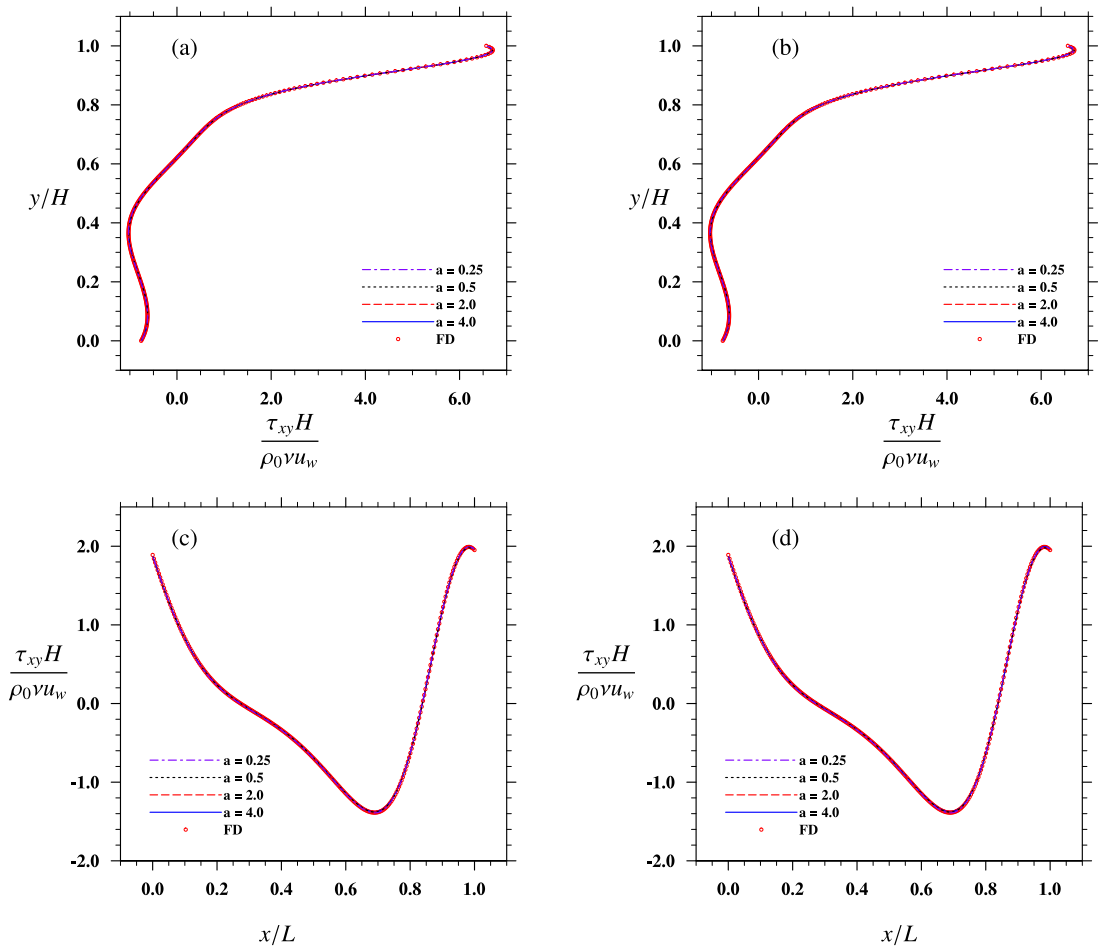

Fig. 12. The shear stress profile along a vertical line ((a) and (b)) and a horizontal line ((c) and (d)) through the geometric center of cavity: (a), (c) τ_{xy}, the present model; (b), (d) τ_{xy}, Bouzidi et al.'s model.

5. Summary and conclusions

In this paper, we have developed a new lattice Boltzmann model on a D2Q9 rectangular grid that is fully consistent with the Navier–Stokes equations. By introducing stress components into the equilibrium moments, the proposed model resolves the remaining anisotropy issue in Bouzidi et al.'s model [28,29]. A detailed Chapman–Enskog analysis was presented to guide an inverse design process. All the relevant equilibrium moments that play a role in shaping the hydrodynamic equations have been determined by matching the N–S equations.

Compared with the θ model [29] that also successfully reproduces the N–S equations on a rectangular grid, the proposed model is more general for the following reasons:

1. First, additional parameters are introduced into the expressions of the bulk viscosity and shear viscosity, making it possible to adjust the values of relevant relaxation times independent of the values of these viscosities. This feature can be used to enhance the numerical stability of the model, especially when the flow Reynolds numbers are high. The additional parameters can handle small viscosities while keeping the relaxation parameters close to one. With this appealing feature, it is also possible to apply the proposed model to the non-Newtonian flow simulations on a rectangular grid.
2. Second, in the θ model the relaxation times (s_e, s_n) for the energy and normal stress moments must be related to the relaxation time (s_c) for the shear stress moment, in order to satisfy the isotropy condition required by the Navier–Stokes equation. These relations are no longer required in the proposed model. This feature makes the proposed model more flexible, namely, the risk of having extreme relaxation parameters due to these relations can now be avoided. Furthermore, without these relations among relaxation parameters, we can set all the relaxation parameters to be identical. This implies the proposed model can be extended to lattice BGK collision operator. This possibility has recently been confirmed [48].

3. Third, the proposed model uses the same moments as in Bouzidi et al.'s model [28], which makes both the derivation and computer implementation of the proposed model simpler than those in the θ model. It is also straightforward to extend the proposed model to a 3D cuboid lattice which has been recently performed by Wang et al. [49].

For the parameters introduced in the proposed model, general guidelines for specifying their values are provided. Even when the grid aspect ratio a, the shear viscosity ν, the bulk viscosity ν^V, the relaxation parameters s_c, s_n, s_e are specified, there are still 2 adjustable parameters c_s and γ in addition to the 4 non-essential free parameters s_q, s_ε, ξ_1 and ξ_2. Therefore, for the proposed model, there are multiple possibilities to determine the parameters. Additional considerations (*e.g.*, numerical stability) may be used to further optimize the parameter settings, which is beyond the scope of the current paper. Future users of the proposed model are encouraged to pursue this direction to maximize the many potential benefits of the model.

To validate the proposed model, we have simulated both the 2D unsteady Taylor–Green vortex flow and the steady lid-driven cavity flow, using different grid aspect ratios. Methods to initialize the mesoscopic distributions and to treat moving solid boundary have been discussed. In all cases, the results from the proposed model are in excellent agreement with either the theoretical solution or benchmark numerical solutions from a high-resolution finite-difference method. The convergence study of the proposed model has also been performed, showing that the model maintains the expected second-order accuracy. The numerical validations discussed in this paper are more complete as we consider not only the accuracy of the simulated velocity field, but also the accuracy of the simulated pressure and stress fields.

Furthermore, the lack of full isotropy of viscosity coefficients in Bouzidi et al.'s model and its consequences are clearly demonstrated by comparing results from Bouzidi et al.'s model to those based on the proposed model and benchmark results. Interestingly, Bouzidi et al.'s model provides accurate results of velocity field and the shear stress for both flows, however, their results for the normal stress and pressure clearly show systematic errors.

Acknowledgements

This work has been supported by the U.S. National Science Foundation (NSF) under grants CNS1513031, CBET-1235974, and AGS-1139743 and by the Air Force Office of Scientific Research under grant FA9550-13-1-0213. LPW also acknowledges support from the Ministry of Education of the People's Republic of China and Huazhong University of Science and Technology through Chang Jiang Scholar Visiting Professorship. Computing resources are provided by National Center for Atmospheric Research through CISL-P35751014 and CISL-UDEL0001 and by University of Delaware through NSF CRI 0958512.

References

[1] H. Tennekes, J.L. Lumley, A First Course in Turbulence, MIT Press, 1972.
[2] R.D. Moser, J. Kim, N.N. Mansour, Direct numerical simulation of turbulent channel flow up to Re = 590, Phys. Fluids 11 (4) (1999) 943–945.
[3] P. Lammers, K. Beronov, R. Volkert, G. Brenner, F. Durst, Lattice BGK direct numerical simulation of fully developed turbulence in incompressible plane channel flow, Comput. Fluids 35 (10) (2006) 1137–1153.
[4] C. Chin, A. Ooi, I. Marusic, H. Blackburn, The influence of pipe length on turbulence statistics computed from direct numerical simulation data, Phys. Fluids 22 (11) (2010) 115107.
[5] X. Shao, T. Wu, Z. Yu, Fully resolved numerical simulation of particle-laden turbulent flow in a horizontal channel at a low Reynolds number, J. Fluid Mech. 693 (2012) 319–344.
[6] J. Kim, P. Moin, R. Moser, Turbulence statistics in fully developed channel flow at low Reynolds number, J. Fluid Mech. 177 (1987) 133–166.
[7] A. Ten Cate, J.J. Derksen, L.M. Portela, H.E. Van Den Akker, Fully resolved simulations of colliding monodisperse spheres in forced isotropic turbulence, J. Fluid Mech. 519 (2004) 233–271.
[8] C.K. Aidun, J.R. Clausen, Lattice-Boltzmann method for complex flows, Annu. Rev. Fluid Mech. 42 (2010) 439–472.
[9] M. Stiebler, M. Krafczyk, S. Freudiger, M. Geier, Lattice Boltzmann large eddy simulation of subcritical flows around a sphere on non-uniform grids, Comput. Math. Appl. 61 (12) (2011) 3475–3484.
[10] L.-P. Wang, O. Ayala, H. Gao, C. Andersen, K.L. Mathews, Study of forced turbulence and its modulation by finite-size solid particles using the lattice Boltzmann approach, Comput. Math. Appl. 67 (2) (2014) 363–380.
[11] L.-P. Wang, C. Peng, Z. Guo, Z. Yu, Lattice Boltzmann simulation of particle-laden turbulent channel flow, Comput. Fluids 124 (2016) 226–236.
[12] D. Yu, R. Mei, W. Shyy, A multi-block lattice Boltzmann method for viscous fluid flows, Int. J. Numer. Methods Fluids 39 (2) (2002) 99–120.
[13] B. Crouse, E. Rank, M. Krafczyk, J. Tölke, A LB-based approach for adaptive flow simulations, Int. J. Mod. Phys. B 17 (01n02) (2003) 109–112.
[14] S. Geller, M. Krafczyk, J. Tölke, S. Turek, J. Hron, Benchmark computations based on lattice-Boltzmann, finite element and finite volume methods for laminar flows, Comput. Fluids 35 (8) (2006) 888–897.
[15] D. Yu, S.S. Girimaji, Multi-block lattice Boltzmann method: extension to 3D and validation in turbulence, Physica A: Stat. Mech. Appl. 362 (1) (2006) 118–124.
[16] J. Tölke, S. Freudiger, M. Krafczyk, An adaptive scheme using hierarchical grids for lattice Boltzmann multi-phase flow simulations, Comput. Fluids 35 (8) (2006) 820–830.
[17] Y. Peng, C. Shu, Y.-T. Chew, X. Niu, X.-Y. Lu, Application of multi-block approach in the immersed boundary–lattice Boltzmann method for viscous fluid flows, J. Comput. Phys. 218 (2) (2006) 460–478.
[18] Z. Xia, K.W. Connington, S. Rapaka, P. Yue, J.J. Feng, S. Chen, Flow patterns in the sedimentation of an elliptical particle, J. Fluid Mech. 625 (2009) 249–272.
[19] M. Dietzel, M. Sommerfeld, Numerical calculation of flow resistance for agglomerates with different morphology by the lattice-Boltzmann method, Powder Technol. 250 (2013) 122–137.
[20] S. Geller, S. Uphoff, M. Krafczyk, Turbulent jet computations based on MRT and cascaded lattice Boltzmann models, Comput. Math. Appl. 65 (12) (2013) 1956–1966.
[21] S. Chen, C. Peng, Y. Teng, L.-P. Wang, K. Zhang, Improving lattice Boltzmann simulation of moving particles in a viscous flow using local grid refinement, Comput. Fluids 22 (2016) 228–246.

[22] X. He, L.-S. Luo, M. Dembo, Some progress in lattice Boltzmann method. Part I. Nonuniform mesh grids, J. Comput. Phys. 129 (2) (1996) 357–363.
[23] X. Niu, Y. Chew, C. Shu, Simulation of flows around an impulsively started circular cylinder by Taylor series expansion- and least squares-based lattice Boltzmann method, J. Comput. Phys. 188 (1) (2003) 176–193.
[24] O. Filippova, D. Hänel, Boundary-fitting and local grid refinement for lattice-BGK models, Int. J. Mod. Phys. C 9 (8) (1998) 1271–1279.
[25] N. Cao, S. Chen, S. Jin, D. Martinez, Physical symmetry and lattice symmetry in the lattice Boltzmann method, Phys. Rev. E 55 (1) (1997) R21.
[26] A. Bardow, I.V. Karlin, A.A. Gusev, General characteristic-based algorithm for off-lattice Boltzmann simulations, Europhys. Lett. 75 (3) (2006) 434.
[27] J. Koelman, A simple lattice Boltzmann scheme for Navier–Stokes fluid flow, Europhys. Lett. 15 (6) (1991) 603.
[28] M. Bouzidi, D. d'Humières, P. Lallemand, L.-S. Luo, Lattice Boltzmann equation on a two-dimensional rectangular grid, J. Comput. Phys. 172 (2) (2001) 704–717.
[29] Y. Zong, C. Peng, Z. Guo, L.-P. Wang, Designing correct fluid hydrodynamics on a rectangular grid using MRT lattice Boltzmann approach, Comput. Math. Appl. 72 (2) (2016) 288–310.
[30] J.G. Zhou, Rectangular lattice Boltzmann method, Phys. Rev. E 81 (2) (2010) 026705.
[31] J.G. Zhou, MRT rectangular lattice Boltzmann method, Int. J. Mod. Phys. C 23 (5) (2012) 1250040.
[32] S. Chikatamarla, I. Karlin, Comment on "Rectangular lattice Boltzmann method", Phys. Rev. E 83 (4) (2011) 048701.
[33] L.A. Hegele Jr., K. Mattila, P.C. Philippi, Rectangular lattice-Boltzmann schemes with BGK-collision operator, J. Sci. Comput. 56 (2) (2013) 230–242.
[34] T. Inamuro, A lattice kinetic scheme for incompressible viscous flows with heat transfer, Philos. Trans. R. Soc., Math. Phys. Eng. Sci. 360 (1792) (2002) 477–484.
[35] M. Yoshino, Y. Hotta, T. Hirozane, M. Endo, A numerical method for incompressible non-Newtonian fluid flows based on the lattice Boltzmann method, J. Non-Newton. Fluid Mech. 147 (1) (2007) 69–78.
[36] L. Wang, J. Mi, X. Meng, Z. Guo, A localized mass-conserving lattice Boltzmann approach for non-Newtonian fluid flows, Commun. Comput. Phys. 17 (4) (2015) 908–924.
[37] X. Meng, Z. Guo, Multiple-relaxation-time lattice Boltzmann model for incompressible miscible flow with large viscosity ratio and high Péclet number, Phys. Rev. E 92 (4) (2015) 043305.
[38] P. Lallemand, L.-S. Luo, Theory of the lattice Boltzmann method: dispersion, dissipation, isotropy, Galilean invariance, and stability, Phys. Rev. E 61 (6) (2000) 6546.
[39] D. d'Humières, Multiple-relaxation-time lattice Boltzmann models in three dimensions, Philos. Trans. R. Soc., Math. Phys. Eng. Sci. 360 (1792) (2002) 437–451.
[40] X. He, L.-S. Luo, Lattice Boltzmann model for the incompressible Navier–Stokes equation, J. Stat. Phys. 88 (3–4) (1997) 927–944.
[41] P.J. Dellar, Bulk and shear viscosities in lattice Boltzmann equations, Phys. Rev. E 64 (3) (2001) 031203.
[42] L.-S. Luo, W. Liao, X. Chen, Y. Peng, W. Zhang, et al., Numerics of the lattice Boltzmann method: effects of collision models on the lattice Boltzmann simulations, Phys. Rev. E 83 (5) (2011) 056710.
[43] R. Mei, L.-S. Luo, P. Lallemand, D. d'Humières, Consistent initial conditions for lattice Boltzmann simulations, Comput. Fluids 35 (8) (2006) 855–862.
[44] W.-A. Yong, L.-S. Luo, et al., Accuracy of the viscous stress in the lattice Boltzmann equation with simple boundary conditions, Phys. Rev. E 86 (6) (2012) 065701.
[45] S. Hou, Q. Zou, S. Chen, G. Doolen, A.C. Cogley, Simulation of cavity flow by the lattice Boltzmann method, J. Comput. Phys. 118 (2) (1995) 329–347.
[46] U. Ghia, K.N. Ghia, C. Shin, High-Re solutions for incompressible flow using the Navier–Stokes equations and a multigrid method, J. Comput. Phys. 48 (3) (1982) 387–411.
[47] J. Kim, P. Moin, Application of a fractional-step method to incompressible Navier–Stokes equations, J. Comput. Phys. 59 (2) (1985) 308–323.
[48] C. Peng, Z. Guo, L.-P. Wang, A lattice-BGK model for the Navier–Stokes equations based on a rectangular grid, Comput. Math. Appl. (2016), http://dx.doi.org/10.1016/j.camwa.2016.05.007.
[49] L.-P. Wang, H. Min, C. Peng, N. Geneva, Z. Guo, A lattice-Boltzmann scheme of the Navier–Stokes equation on a three-dimensional cuboid lattice, Comput. Math. Appl. (2016), http://dx.doi.org/10.1016/j.camwa.2016.06.017.